

# Modeling of complex actuation modalities in transitional boundary layers

Research project

Ofek Frank-Shapir

Advisor - Igal Gluzman

Faculty of Aerospace Engineering

Technion - Israel Institute of Technology

February 26, 2024

## Abstract

Predicting the resulting flow field due to external forcing is highly important in designing feedback controllers in active flow control applications and studying the flow physics of boundary layers subject to external forcing. We have developed an input-output solver based on linearized Navier-stokes equations to capture structural features and energy pathways of transitional wall-bounded shear flows. We extended our input-output solver to model the flow response to actuation following Gluzman and Gayme, 2021a approach, where the actuator geometry was represented as a cluster of single-point source arrays arranged in an actuator's geometrical pattern. Lastly, we propose a novel simplified model for determining the optimal spacing between a spanwise array of symmetric plasma actuators for maximal amplification of the streamwise velocity component via generation spanwise-periodic counter-rotating vortices. Our modeling tool can be utilized in designing and optimizing actuation patterns in active flow control applications at a fraction of the time compared to high-fidelity simulations.

## 1 Introduction

Being able to predict the resulting flow field due to actuation is of high importance in designing feedback controllers in active flow control applications and studying the flow physics of boundary layers that are subject to external forcing. In the reduced modeling approach, simplifications for the governing equations are usually used to approximate the high-dimensional system that retains those aspects of the flow that are relevant from a control perspective Kim and Bewley, 2007; Taira et al., 2017. Hydrodynamic stability and input-output-analysis-based tools have shown great promise in providing the required understanding. In particular, the externally forced linearized Navier-Stokes (LNS) system has shown success in examining the important dynamic processes, structural features, and energy pathways of transitional e.g., Jovanović and Bamieh, 2005a and turbulent e.g., Hwang and Cossu, 2010 wall-bounded shear flows. In flow control applications, input-output-based

analysis has been used to derive control laws e.g., Semeraro et al., 2013 and preliminary assessment of actuation strategies e.g., Tol et al., 2019. These methods have also been adapted to analyze the effect of flow manipulation limited to temporal periodic actuation, such as transverse wall oscillations Moarref and Jovanović, 2010, surface blowing and suction Moarref and Jovanović, 2012; and spatially periodic passive actuation configurations, such as different riblet shapes for drag reduction in turbulent channel flow Chavarin and Luhar, 2019. On the other hand, it is more common in experimental flow control to find many other types of actuators, such as plasma actuators Thomas et al., 2019. Plasma actuators have no moving parts, are very light and thin, and can operate at a wide range of frequency bands, making them suitable for use over flight speeds up to 3.5 Mach, at which their utilization has demonstrated staggering 70% reduction of drag. These actuators come in a variety of configurations and can be operated under pulsed excitation with adjustable duty cycle and frequency. These actuators introduce localized input that is typically modeled as a body force distribution in physical space Morra et al., 2020.

In Gluzman and Gayme, 2021a, an input-output approach is used to compute the flow response to specific localized plasma actuator geometries. The approach takes advantage of the linearity of the transfer function representation to construct the actuated flow field as a weighted superposition of the flow responses to point sources of varying intensity comprising the actuation model. The approach has been successfully applied in transitional flows and validated for the special case of step input signals, which provide a model for continuous actuation signals. This input class provides an important test case as the associated flow response corresponds to the time-averaged flow field due to constant actuation, which is extensively reported in the literature. Still, utilizing this framework for actuators design and optimization has not been considered yet.

In this work, we derive an input-output LNS solver to study the flow physics of the flow response to external forcing and propose a novel approach for designing and optimizing actuators, focusing on a spanwise periodic array of plasma actuators. In the first part of this report, we validated our LNS input-output solver via reproducing the results from M. R. Jovanovic, 2004, Jovanović and Bamieh, 2005b and Gluzman and Gayme, 2021b, focusing on amplification of perturbations, their energy pathways in plane channel flow and Blasius boundary layer. In the second part, we propose a simplified approach to study the flow response to the spanwise plasma actuator array that was utilized in the experimental setup taken from Hanson et al., 2010 for the Blasius boundary layer. A single wave number pair is used to determine the optimal wave number combination for achieving maximal amplification of streamwise velocity perturbations. This approach can determine the optimized spanwise spacing of the plasma actuator array in a fraction of the time that it takes with a regular input-output approach of Gluzman and Gayme, 2021a.

The rest of this project is organized in the following order: Analytic model derivation is presented in section 2. Results are presented and validated in section 3. Finally, conclusions and areas of future development are discussed in section 4.

## 2 Analytic Model

We consider incompressible, Wall-bounded parallel shear flow, for which the linearized Navier-Stokes equations for perturbations in fluid velocity and pressure  $(\mathbf{u}, p)$  about the

base flow  $(\bar{\mathbf{u}}, \bar{p})$  are as follows:

$$\begin{aligned} \frac{\partial \mathbf{u}}{\partial t} &= -\bar{\mathbf{u}}(\nabla \mathbf{u}) - \mathbf{u}(\nabla \bar{\mathbf{u}}) - \nabla p + \frac{1}{Re} \Delta \mathbf{u} + \mathbf{d}, \\ \nabla \cdot \mathbf{u} &= 0. \end{aligned} \quad (1)$$

Here,  $\mathbf{u} = [u, v, w]^T$  is the velocity perturbation vector, corresponding to the streamwise  $x$ , wall normal  $y$ , and spanwise  $z$  directions, respectively;  $\mathbf{d} = [d_x, d_y, d_z]^T$  is the term representing body forcing.  $\nabla$  is the Nabla operator and  $\Delta = \nabla^2$  is the Laplacian operator. We apply the Laplacian operator to the equation for  $v$ , using the definition of the vorticity vector. In addition, spatial invariance of the parallel flow field in the horizontal directions, allows performing Fourier transforms in the  $x$  and  $z$  directions provides a system of 2 ODEs in the variable  $y$  (Kim et al., 1987). This process allows to write the LNS equations in a state-space form, which easier to perform input-output analysis on, as done in Jovanović and Bamieh, 2005b:

$$\begin{aligned} \frac{\partial \psi}{\partial t}(k_x, y, k_z, t) &= [\mathcal{A}(k_x, k_z) \boldsymbol{\psi}(k_x, y, k_z, t)](y) + [\mathcal{B}(k_x, k_z) \mathbf{d}(k_x, k_z, t)](y), \\ \phi(k_x, y, k_z, t) &= \mathcal{C}(k_x, k_z) \boldsymbol{\psi}(k_x, k_z, t)(y), \end{aligned} \quad (2)$$

where  $\boldsymbol{\psi} \equiv [v, \omega_y]^T$  and  $\boldsymbol{\phi} \equiv \mathbf{u} = [u, v, w]^T$ . These equations containing only the wall-normal velocity perturbation  $v$ , the perturbation in wall-normal vorticity  $\omega_y = \frac{\partial u}{\partial z} - \frac{\partial w}{\partial x}$  and the forcing term  $\mathbf{d}$ . The choice of making the velocity perturbation vector the output of the system was done entirely for convenience and any combination of perturbation variables could have been chosen theoretically. The operators denoted as  $\mathcal{A}$ ,  $\mathcal{B}$  and  $\mathcal{C}$  are defined below for a base velocity profile of the form  $\bar{\mathbf{u}} = [U(y), 0, 0]^T$ :

$$\mathcal{A} \equiv \begin{bmatrix} \mathcal{A}_{11} & 0 \\ \mathcal{A}_{21} & \mathcal{A}_{22} \end{bmatrix} \equiv \begin{bmatrix} -ik_x \Delta^{-1} U \Delta + ik_x \Delta^{-1} U'' + \frac{1}{Re} \Delta^{-1} \Delta^2 & 0 \\ -ik_z U' & -ik_x U + \frac{1}{Re} \Delta \end{bmatrix}, \quad (3)$$

$$\mathcal{B} \equiv [\mathcal{B}_x \quad \mathcal{B}_y \quad \mathcal{B}_z] \equiv \begin{bmatrix} \Delta^{-1} & 0 \\ 0 & I \end{bmatrix} \begin{bmatrix} -ik_x \frac{\partial}{\partial y} & -(k_x^2 + k_z^2) & -ik_z \frac{\partial}{\partial y} \\ ik_z & 0 & -ik_x \end{bmatrix}, \quad (4)$$

$$\mathcal{C} \equiv \begin{bmatrix} \mathcal{C}_u \\ \mathcal{C}_v \\ \mathcal{C}_w \end{bmatrix} \equiv \frac{1}{k_x^2 + k_z^2} \begin{bmatrix} ik_x \frac{\partial}{\partial y} & -ik_z \\ k_x^2 + k_z^2 & 0 \\ ik_z \frac{\partial}{\partial y} & ik_x \end{bmatrix}. \quad (5)$$

Here,  $U' = \frac{dU(y)}{dy}$  and  $U'' = \frac{d^2U(y)}{dy^2}$ . The Laplacian operator is defined as  $\Delta = \frac{\partial^2}{\partial y^2} - (k_x^2 + k_z^2)$  because of the Fourier transforms done in directions  $x$  and  $z$ . All the derivations to obtain the state-space form in Eq. (2) are found in appendix A. We separate the spatial and temporal dependence of the forcing term by using a spatial weighting matrix  $\mathbf{W}$  in the following manner:

$$\mathbf{d}(k_x, y, k_z, t) = \mathbf{W}(k_x, y, k_z) \tilde{\mathbf{d}}(t), \quad (6)$$

where  $\tilde{\mathbf{d}}(t) = [\tilde{d}_x(t), \tilde{d}_y(t), \tilde{d}_z(t)]^T$  represents only the temporal dependence of the forcing term  $\mathbf{d}$ . The spatial weighting matrix  $\mathbf{W}$  is defined as:

$$\mathbf{W}(k_x, y, k_z) = \begin{bmatrix} f(k_x, y, k_z) & 0 & 0 \\ 0 & g(k_x, y, k_z) & 0 \\ 0 & 0 & h(k_x, y, k_z) \end{bmatrix}. \quad (7)$$

Here,  $f(k_x, y, k_z)$ ,  $g(k_x, y, k_z)$  and  $h(k_x, y, k_z)$  are functions that scale the amplitude of each forcing component ( $f$  scales  $\tilde{d}_x$ ,  $g$  scales  $\tilde{d}_y$  and  $h$  scales  $\tilde{d}_z$ ) as a function of the spatial wave numbers  $k_x$  and  $k_z$  and as a function of  $y$ , the position in the wall normal direction. We note that in the most general case there is no dependence between  $f$ ,  $g$  and  $h$ . However, we will only use diagonal weighting matrices which correspond to equal scaling of all forcing components.

## 2.1 Frequency Response

In this section, we consider a forcing term  $\mathbf{d}$ , which is independent of  $y$  direction and harmonic in the temporal sense and in the  $x$  and  $z$  directions. The spatial weighting matrix for such a forcing is:

$$\mathbf{W}(k_x, k_z) = \delta(k_x - \bar{k}_x, k_z - \bar{k}_z) \mathbf{I}_{3 \times 3}. \quad (8)$$

$\mathbf{I}_{3 \times 3}$  is a  $3 \times 3$  identity matrix and  $\bar{k}_x, \bar{k}_z$  are the specific wave numbers that the forcing has in directions  $x$  and  $z$  respectively.  $\delta$  is the Dirac's delta function in 2D and Thus, the term  $\delta(k_x - \bar{k}_x, k_z - \bar{k}_z)$  is the result of the fact that the forcing is harmonic and has wave numbers  $\bar{k}_x$  and  $\bar{k}_z$ . The Temporal dependence of the forcing term is manifested in the condition:

$$|\tilde{\mathbf{d}}(t)| = \sin(\bar{\omega}t), \quad (9)$$

where  $\bar{\omega}$  is the temporal frequency of the forcing term. Assuming stability of operator  $\mathcal{A}$  (which is guaranteed for both Poiseuille and Blasius base flows under laminar flow assumption), the solution to Eq. (2) to a harmonic term described in equations 8 and 9 is:

$$\phi(x, z, t) = \mathcal{H}(k_x, k_z, \omega) \mathbf{W}(k_x, k_z) \tilde{\mathbf{d}}(\omega). \quad (10)$$

In Eq. (10), the operator  $\mathcal{H}(k_x, k_z, \omega)$  is the transfer function from the harmonic forcing term applied to the system to the velocity field that arises, and is given by (Zhou et al., 1995):

$$\mathcal{H}(k_x, k_z, \omega) = \mathcal{C}(k_x, k_z) (i\omega I - \mathcal{A}(k_x, k_z))^{-1} \mathcal{B}(k_x, k_z). \quad (11)$$

It is important to note that the operator  $\mathcal{H}$  in Eq. (11) is valued at a single point along the wall normal direction  $y$ . The reason for that is the dependence of  $\mathcal{A}$  on the base flow, which is a function of  $y$ . As can be seen in equations 4 and 5, the operators  $\mathcal{B}$  and  $\mathcal{C}$  has 3 components each corresponding to different inputs and outputs respectively. This means that  $\mathcal{H}$  can be decomposed in several different ways. Firstly, by considering all components of  $\mathcal{B}$  and  $\mathcal{C}$  we get the following:

$$\begin{aligned} \mathcal{H}(k_x, k_z, \omega) &= \begin{bmatrix} \mathcal{C}_u \\ \mathcal{C}_v \\ \mathcal{C}_w \end{bmatrix} (i\omega I - \mathcal{A}(k_x, k_z))^{-1} \begin{bmatrix} \mathcal{B}_x & \mathcal{B}_y & \mathcal{B}_z \end{bmatrix} \equiv \\ &\equiv \begin{bmatrix} \mathcal{H}_{ux}(k_x, k_z, \omega) & \mathcal{H}_{uy}(k_x, k_z, \omega) & \mathcal{H}_{uz}(k_x, k_z, \omega) \\ \mathcal{H}_{vx}(k_x, k_z, \omega) & \mathcal{H}_{vy}(k_x, k_z, \omega) & \mathcal{H}_{vz}(k_x, k_z, \omega) \\ \mathcal{H}_{wx}(k_x, k_z, \omega) & \mathcal{H}_{wy}(k_x, k_z, \omega) & \mathcal{H}_{wz}(k_x, k_z, \omega) \end{bmatrix}. \end{aligned} \quad (12)$$

This decomposition allows to examine the relationship between specific inputs (forcing in different directions) and outputs (different velocity components). For example,  $\mathcal{H}_{uy}$  is the

operator between forcing in the  $y$  direction and the  $u$  velocity component, which is the component in the  $x$  direction. Other decompositions can be obtained by combining rows or columns of the  $3 \times 3$  matrix in Eq. (12):

$$\mathcal{H}(k_x, k_z, \omega) = \mathcal{C}(i\omega I - \mathcal{A}(k_x, k_z))^{-1} [\mathcal{B}_x \quad \mathcal{B}_y \quad \mathcal{B}_z] \equiv \quad (13)$$

$$\equiv [\mathcal{H}_x(k_x, k_z, \omega) \quad \mathcal{H}_y(k_x, k_z, \omega) \quad \mathcal{H}_z(k_x, k_z, \omega)],$$

$$\mathcal{H}(k_x, k_z, \omega) = \begin{bmatrix} \mathcal{C}_u \\ \mathcal{C}_v \\ \mathcal{C}_w \end{bmatrix} (i\omega I - \mathcal{A}(k_x, k_z))^{-1} \mathcal{B} \equiv \quad (14)$$

$$\equiv \begin{bmatrix} \mathcal{H}_u(k_x, k_z, \omega) \\ \mathcal{H}_v(k_x, k_z, \omega) \\ \mathcal{H}_w(k_x, k_z, \omega) \end{bmatrix}.$$

The decompositions above describe the dynamics between a specific type of forcing and the entire velocity field or the dynamics between forcing in all 3 direction and a specific velocity component. For example,  $\mathcal{H}_x$  is the operator between the  $d_x$  forcing component and the entire velocity field and  $\mathcal{H}_u$  is the operator between forcing in all three directions to the  $u$  component of the velocity field. From here on, we refer to the operators in equations 12, 13 and 14 as sub-operators of the  $\mathcal{H}$  operator. To quantify the idea of amplification of specific frequencies we use the  $\|\cdot\|_2$  norm which is defined in the following manner:

$$\|\mathcal{H}(k_x, k_z, \omega)\|_2^2 \equiv \frac{1}{2\pi} \int_{-\infty}^{\infty} \text{trace}[\mathcal{H}(k_x, k_z, \omega)\mathcal{H}^*(k_x, k_z, \omega)]d\omega. \quad (15)$$

Here,  $*$  denotes the adjoined operator, which is defined the same as in Jovanović and Bamieh, 2005b, under the following inner product:

$$\langle \psi_1, \psi_2 \rangle_e \equiv \langle \psi_1, \mathcal{Q}\psi_2 \rangle = \int_{-1}^1 \psi_1 \cdot \mathcal{Q}\psi_2 dy, \quad (16)$$

where the operator  $\mathcal{Q}$  is defined as follows:

$$\mathcal{Q} \equiv \frac{1}{k_x^2 + k_z^2} \begin{bmatrix} -\Delta & 0 \\ 0 & I \end{bmatrix}. \quad (17)$$

Under the inner product in 16, the adjoint of an operator is defined for an operator  $\mathcal{G}$  using the following relation:

$$\langle \psi_1, \mathcal{G}\psi_2 \rangle_e = \langle \mathcal{G}^*\psi_1, \psi_2 \rangle_e. \quad (18)$$

Using Eq. (18) and substituting  $\mathcal{G}$  with the operators  $\mathcal{A}$ ,  $\mathcal{B}$ ,  $\mathcal{C}$  we can get relations between them and their adjoint operators:

$$\begin{aligned} \langle \psi_1, \mathcal{A}\psi_2 \rangle_e &= \langle \mathcal{A}^*\psi_1, \psi_2 \rangle_e, \\ \langle \psi, \mathcal{B}\mathbf{d} \rangle_e &= \langle \mathcal{B}^*\psi, \mathbf{d} \rangle_e, \\ \langle \phi, \mathcal{C}\psi \rangle_e &= \langle \mathcal{C}^*\phi, \psi \rangle_e. \end{aligned} \quad (19)$$

Using these relations we can solve for  $\mathcal{A}^*$ ,  $\mathcal{B}^*$ ,  $\mathcal{C}^*$  and get:

$$\mathcal{A}^* \equiv \begin{bmatrix} \mathcal{A}_{11}^* & \mathcal{A}_{12}^* \\ 0 & \mathcal{A}_{22}^* \end{bmatrix} \equiv \begin{bmatrix} ik_x U - ik_x \Delta^{-1} U'' + \frac{1}{Re} \Delta^{-1} \Delta^2 & -ik_z \Delta^{-1} U' \\ 0 & ik_x U + \frac{1}{Re} \Delta \end{bmatrix}, \quad (20)$$

$$\mathcal{B}^* \equiv \begin{bmatrix} \mathcal{B}_x^* \\ \mathcal{B}_y^* \\ \mathcal{B}_z^* \end{bmatrix} \equiv \frac{1}{k_x^2 + k_z^2} \begin{bmatrix} ik_x \frac{\partial}{\partial y} & -ik_z \\ k_x^2 + k_z^2 & 0 \\ ik_z \frac{\partial}{\partial y} & ik_x \end{bmatrix}, \quad (21)$$

$$\mathcal{C}^* \equiv [\mathcal{C}_u^* \quad \mathcal{C}_v^* \quad \mathcal{C}_w^*] \equiv \begin{bmatrix} \Delta^{-1} & 0 \\ 0 & I \end{bmatrix} \begin{bmatrix} -ik_x \frac{\partial}{\partial y} & -(k_x^2 + k_z^2) & -ik_z \frac{\partial}{\partial y} \\ ik_z & 0 & -ik_x \end{bmatrix}. \quad (22)$$

Herein,  $\mathcal{B}_x^* = \mathcal{C}_u$ ,  $\mathcal{B}_y^* = \mathcal{C}_v$ ,  $\mathcal{B}_z^* = \mathcal{C}_w$  and  $\mathcal{C}_u^* = \mathcal{B}_x$ ,  $\mathcal{C}_v^* = \mathcal{B}_y$ ,  $\mathcal{C}_w^* = \mathcal{B}_z$ . Thus, we can state that  $\mathcal{B}^* = \mathcal{C}$  and  $\mathcal{C}^* = \mathcal{B}$ . We can use the adjoint operators  $\mathcal{A}^*$ ,  $\mathcal{B}^*$ ,  $\mathcal{C}^*$  to find the  $\mathcal{H}_2$  norm defined in Eq. (15) without finding  $\mathcal{H}^*$  and without solving the integral directly. To do that, we Use the concepts of Controllability and observability Gramians in the frequency domain, as defined in Aghaee et al., 2003. It can be shown that:

$$\begin{aligned} \|\mathcal{H}(k_x, k_z, \omega)\|_2^2 &= \text{trace}[\mathcal{C}(k_x, k_z) \mathcal{X}(k_x, k_z) \mathcal{C}^*(k_x, k_z)] = \\ &= \text{trace}[\mathcal{B}(k_x, k_z) \mathcal{Y}(k_x, k_z) \mathcal{B}^*(k_x, k_z)], \end{aligned} \quad (23)$$

where  $\mathcal{X}$  is the Controllability Gramian and  $\mathcal{Y}$  is the observability Gramian. We note that Eq. (23) is different then the one presented in Jovanović and Bamieh, 2005b. The version written here is the correct one, as showed in Zhou et al., 1995 and as written in later articles (for example, Jovanović, 2021). It is also shown in Zhou et al., 1995 that linear systems of the form in Eq. (2), the controllability and observability Gramians can be calculated using the following Lyapunov equations:

$$\begin{aligned} \mathcal{A}(k_x, k_z) \mathcal{X}(k_x, k_z) + \mathcal{X}(k_x, k_z) \mathcal{A}^*(k_x, k_z) &= -\mathcal{B}(k_x, k_z) \mathcal{B}^*(k_x, k_z), \\ \mathcal{A}^*(k_x, k_z) \mathcal{Y}(k_x, k_z) + \mathcal{Y}(k_x, k_z) \mathcal{A}(k_x, k_z) &= -\mathcal{C}^*(k_x, k_z) \mathcal{C}(k_x, k_z). \end{aligned} \quad (24)$$

This means that using equations (23) and (24), it is possible to find the value of  $\|\mathcal{H}\|_2$  without computing the integral in Eq. (15) but only by solving the Lyapunov equations, which can be done numerically in a variety of ways. As mentioned before, the  $\mathcal{H}$  operator is the transfer function between forcing and velocity. Thus, the quantity  $\|\mathcal{H}\|_2^2$  represents the square of the gain of the system. This can be interpreted in 2 ways: Firstly, the quantity  $\|\mathcal{H}\|_2^2$  is a measure for how much perturbations in velocity get amplified for a given forcing magnitude. Secondly,  $\|\mathcal{H}\|_2^2$  can also be interpreted as the gain between the forcing term and the quantity  $\frac{1}{2}|\mathbf{u}|^2$ . This term represents the kinetic energy density of the perturbations in the flow. Of course, the mentioned interpretation is valid for all forcing directions and for all the velocity components, corresponding to a specific  $\mathcal{H}$  sub-operator. It is important to add that the norms of all the  $\mathcal{H}$  sub-operators can BE calculated similarly to the  $\mathcal{H}_2$  norm by using the corresponding  $\mathcal{B}$  and  $\mathcal{C}$  sub-operators. For example, for calculating  $\|\mathcal{H}_{ux}\|_2$  we substitute  $\mathcal{B}$  and  $\mathcal{C}$  with  $\mathcal{B}_x$  and  $\mathcal{C}_u$ .

## 2.2 Temporal Response and Actuator Modeling

In this section we consider non-periodic response in time and is localized around a specific height in the wall normal direction. The spatial weighting matrix in this case is:

$$\mathbf{W}(y) = \gamma(y)\mathbf{I}_{3 \times 3}. \quad (25)$$

Here,  $\gamma(y)$  is used to model forcing in a specific height above the wall (meaning, in a specific  $y$  coordinate) and is a Gaussian function with a mean of  $y_0$  variance of  $2\varepsilon$ . This approach is the same as in M. Jovanovic and Bamieh, 2001, and yields the following expression:

$$\gamma(y) = \frac{1}{2\sqrt{\pi\varepsilon}} e^{-(y-y_0)^2/4\varepsilon}, \varepsilon > 0. \quad (26)$$

In this section, we are interested in the response for impulse and step temporal inputs. The general temporal solutions to Eq. (2) assuming stability of operator  $\mathcal{A}$  and no perturbations when  $t = 0$  is (Hespanha, 2018):

$$\phi(k_x, y, k_z, t) = \mathcal{C}(k_x, k_z) \int_0^t e^{\mathcal{A}(k_x, k_z)\tau} \mathcal{B}(k_x, k_z) \mathbf{W}(y) \tilde{\mathbf{d}}(\tau) d\tau. \quad (27)$$

Firstly, for an impulse forcing term of the form  $\tilde{\mathbf{d}} = \delta(t)$  The solutions is:

$$\phi(k_x, y, k_z, t) = \mathcal{C}(k_x, k_z) e^{\mathcal{A}(k_x, k_z)t} \mathcal{B}(k_x, k_z) \mathbf{W}(y). \quad (28)$$

For a unit step forcing of the form  $\tilde{\mathbf{d}} = H(t)$  the steady-state solution is:

$$\phi_{ss}(k_x, y, k_z) = -\mathcal{C}(k_x, k_z) \mathcal{A}^{-1}(k_x, k_z) \mathcal{B}(k_x, k_z) \mathbf{W}(y), \quad (29)$$

where  $\delta(t)$  is the Dirac delta function and  $H(t)$  is a unit step function. To control the location of the applied forcing in the  $(x, z)$  plane, we exploit the shift theorem for Fourier transform (Smith, 2008). According to the shift theorem, if we have a forcing term in location  $s_1 = (x_1, z_1)$  and we shift it to location  $s_2 = (x_1 + \Delta x, z_1 + \Delta z)$ , then the solution with the shifted term will be shifted as well and will satisfy the following condition:

$$\phi(k_x, y, k_z, t|s_2) = \phi(k_x, y, k_z, t|s_1) \cdot e^{-i(k_x \Delta x + k_z \Delta z)}. \quad (30)$$

One of our objectives is to model the response for a plasma actuator inside a boundary layer. We can use this fact to model every forcing geometry by an array of densely spaced point sources, similarly to the work done in Gluzman and Gayme, 2021b. The solution after combining all the point sources is:

$$\phi(k_x, y, k_z, t) = \frac{1}{N_s} \sum_{m=1}^{N_s} [e^{-i(k_x \Delta x + k_z \Delta z)} c_m \sum_{j=x,y,z} e_{d,j}(m) \phi_j(k_x, y, k_z, t|s_m)]. \quad (31)$$

Here,  $N_s$  is the number of point sources used,  $c_m$  is a weighting function representing the magnitude of each point source and  $e_d$  is a unit vector representing the forcing direction for each source.

### 3 Results

This section is organized as follows: first, we calculate norms for the  $\mathcal{H}$  operator and all of the sub-operators described in Eqs. (12), (13), and (14). We perform this calculation for both Poiseuille and Blasius base flows. Then, we calculate the steady-state temporal response of Blasius base flow to the plasma actuator array setup used in Belson et al., 2012, using Eq. (29). Lastly, we decompose the mentioned setup to 2 problems with a corresponding pair of wave numbers for each one and demonstrate the accuracy of this method for predicting the optimal wave number pair for maximal amplification of the streamwise velocity component.

To compute the operators in Eq. (2) and the flow field they produce, we apply discretization to the wall-normal direction by using Chebyshev collocation points. We implement this discretization process by using the pseudo spectral differentiation matrices in Weideman and Reddy, 2000 for differentiation in the wall-normal direction. All of the calculations are performed in MATLAB® R2022a and the forcing is applied closest to the wall. This means that the value of  $y_0$  in Eq. (26) is the one that translate to the closest point to the wall in the  $y$  axis. This value changes according to  $N$ , the number of Chebyshev collocation points chosen. A value of  $\varepsilon = 10^{-4}$  was used to calculate  $\gamma(y)$  in Eq. (26) and to obtain all of the results as it was sufficiently small to achieve identical results to M. Jovanovic and Bamieh, 2001 and Jovanović and Bamieh, 2005b.

#### 3.1 Energy Amplification

In this section we consider Poiseuille and Blasius base flow profiles and calculate the  $\mathcal{H}_2$  norms for each base profile. As mentioned in Section 2,  $\|\mathcal{H}\|_2^2$  is the amplification of the kinetic energy density, which will be referred to as energy amplification for simplicity. We apply the method used in Jovanović and Bamieh, 2005b to calculate the norms from body forces to velocity fields in all directions in 3D, as a function of wave numbers in the spanwise and streamwise directions. The results are used for both purposes: to validate our numerical solver with existing results from the literature, and for obtaining intuition about the flow physics of the disturbance fields with respect to the considered canonical base flows.

##### 3.1.1 Poiseuille flow

In this section, we present results of application our input-output LNS solver for plane Poiseuille base flow profile of the form  $U = 1 - y^2$ . To compute the  $\mathcal{H}_2$  norms, Eq. (24) was solved, where the wall normal domain was represented using  $N = 29$  Chebyshev collocation points; and for the horizontal wave-number domain, we used a  $50 \times 90$  grid of logarithmically spaced values with the following boundaries: ( $k_{x_{min}} = 10^{-4}$ ,  $k_{x_{max}} = 3.02$ ) and ( $k_{z_{min}} = 10^{-2}$ ,  $k_{z_{max}} = 15.84$ ). This is the same grid used in Jovanović and Bamieh, 2005b. The obtained  $\|\mathcal{H}_{rs}(k_x, k_z)\|$  norms, where  $r = \{u, v, w\}$  and  $s = \{x, y, z\}$ , are illustrated in figure 1. These norms represent amplification of single velocity component by a single forcing component. Our plots are validated with figure 2 that we reproduced from Jovanović and Bamieh, 2005b. All results are presented on a logarithmic scale.

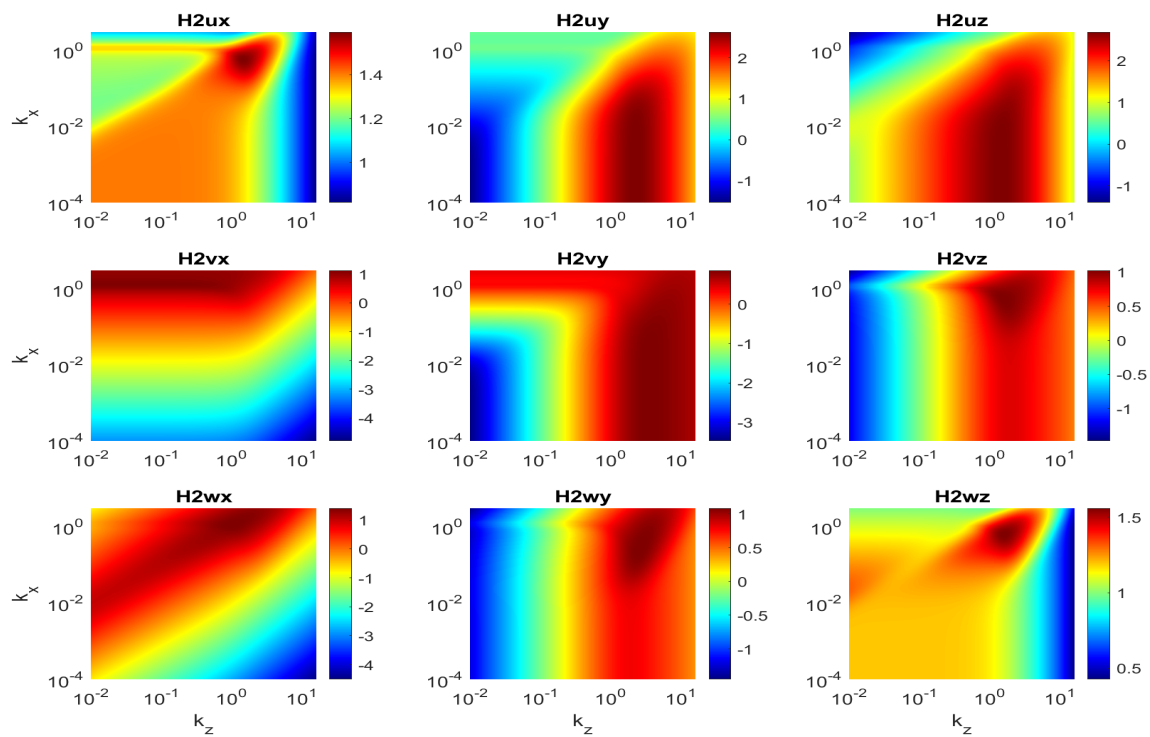


Figure 1: Plots of  $\|\mathcal{H}_{rs}\|_2(k_x, k_z)$  in Poiseuille flow with  $Re = 2000$ .

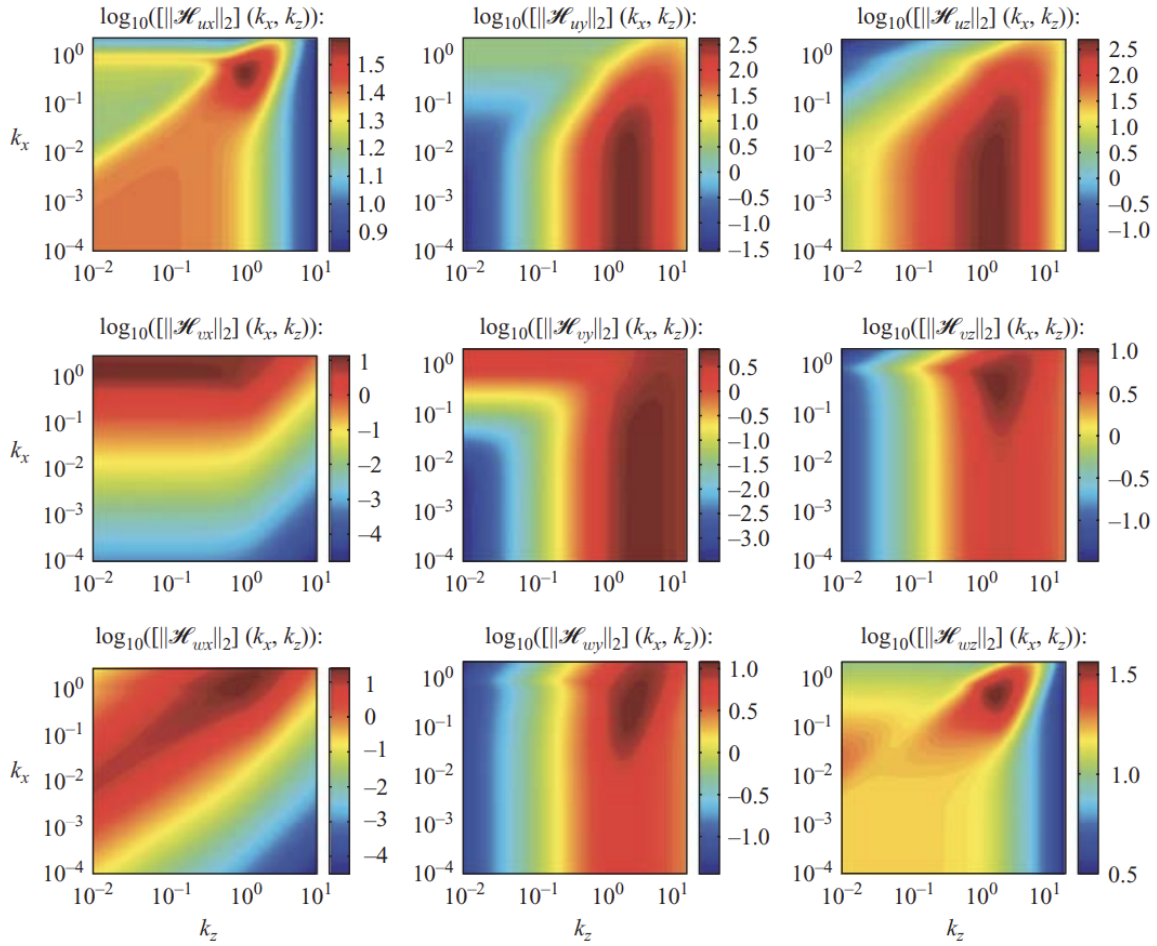


Figure 2: Plots of  $\|\mathcal{H}_{rs}\|_2(k_x, k_z)$  in Poiseuille flow with  $Re = 2000$ , Reprinted from Fig. 2, Jovanović and Bamieh, 2005b.

Several physical insights revealed from figure 1. First, the strongest amplification occurs in the components  $\|\mathcal{H}_{uy}\|_2$  and  $\|\mathcal{H}_{uz}\|_2$ , i.e. from forcing in the spanwise and wall normal directions to the streamwise velocity component  $u$ . These modes of amplification are strongest when  $k_x = 0$  and  $k_z \approx O(1)$ . The amplification of the spanwise and wall normal velocity components ( $v, w$ ) is of order of magnitude weaker than the amplification of  $u$ . There are 3 primary modes of amplification that are evident: 2D TS waves mode - characterized by  $k_x \approx O(1)$  and  $k_z = 0$ . This mode corresponds to a horizontal line of high amplification near the top of the plots in figure 1. Oblique waves mode - characterized by  $k_x \approx O(1)$  and  $k_z \approx O(1)$ . This mode corresponds to a small region of high amplification near the top right corner of the plots in figure 1. Streaks mode - characterized by  $k_x = 0$  and  $k_z \approx O(1)$ . This mode corresponds to a vertical line of high amplification near the right border of the plots in figure 1 and is clearly evident in subplot for  $\|\mathcal{H}_{2ux}\|$ .

Each of these modes is the dominant one for some of the  $\mathcal{H}$  sub-operators. In detail, the streaks mode is dominant in the norms of  $\mathcal{H}_{uy}$ ,  $\mathcal{H}_{uz}$  and for  $\mathcal{H}_{vy}$ . The oblique waves mode is the dominant one for all the sub-operators related to the  $w$  velocity component ( $\mathcal{H}_{wx}$ ,  $\mathcal{H}_{wy}$ ,  $\mathcal{H}_{wz}$ ), demonstrating how distinct the oblique waves mode is in amplification of spanwise perturbations. The TS waves mode is apparent in some of the norms but dominates only for  $\mathcal{H}_{vx}$ . The main physical intuition from the above results is that for  $u$  and  $v$

the strongest amplification is achieved by using forcing in a perpendicular direction to the velocity component. For maximal amplification of the spanwise velocity  $w$ , results due to forcing in an angle of around  $45^\circ$  (oblique wave).

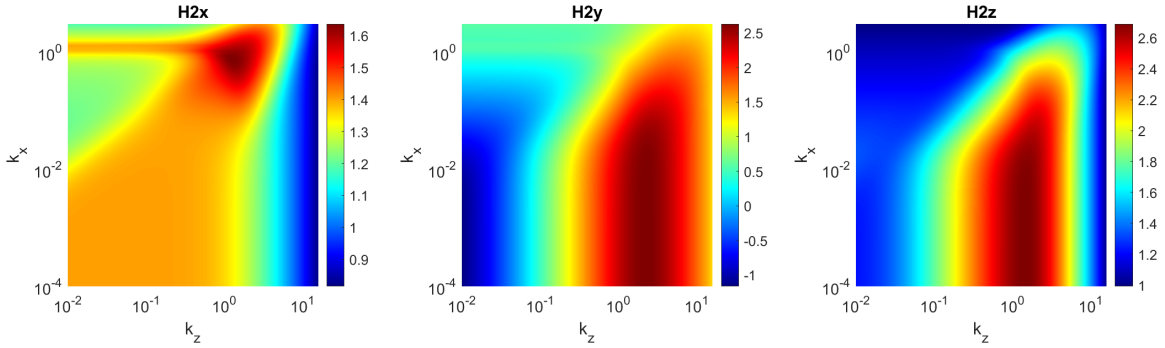


Figure 3: Plots of  $\|\mathcal{H}_x\|_2(k_x, k_z)$ ,  $\|\mathcal{H}_y\|_2(k_x, k_z)$ ,  $\|\mathcal{H}_z\|_2(k_x, k_z)$  in Poiseuille flow with  $Re = 2000$ .

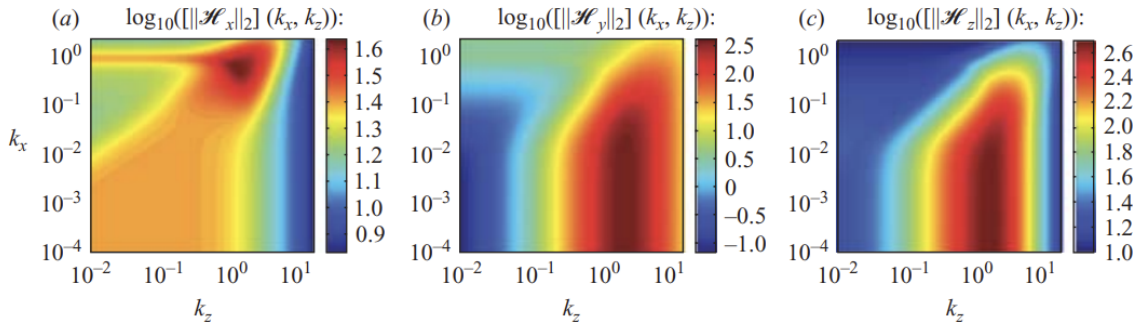


Figure 4: Plots of  $\|\mathcal{H}_x\|_2(k_x, k_z)$ ,  $\|\mathcal{H}_y\|_2(k_x, k_z)$ ,  $\|\mathcal{H}_z\|_2(k_x, k_z)$  in Poiseuille flow with  $Re = 2000$ , Reprinted from Fig. 3, Jovanović and Bamieh, 2005b.

Energy amplification of each forcing direction is illustrated in figure 3. Figure 4 shows the same results taken from Jovanović and Bamieh, 2005b for the same  $\mathcal{H}_2$  norms, showing that we accurately reproduce these plots with our solver. The main conclusion evident from these plots is that the most amplified mode for forcing in the  $x$ -direction is an oblique TS wave mode, while forcing in the  $y$  and  $z$  directions are most amplified when the forcing is done such that  $k_x = 0$  and  $k_z \approx O(1)$ . The  $z$ -direction forcing can reach the highest amplification, followed closely by the  $y$  direction forcing. The response due to forcing in the  $x$ -direction reaches an amplification 10 times smaller than amplification in the  $y$  and  $z$  directions.

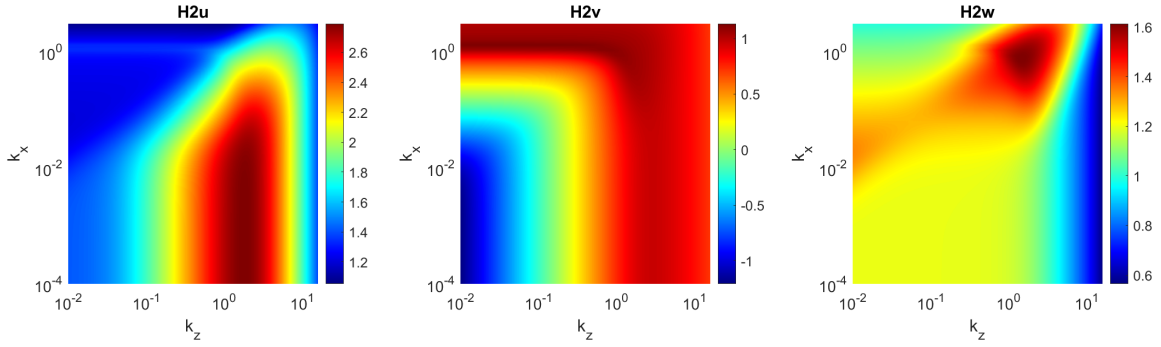


Figure 5: Plots of  $\|\mathcal{H}_u\|_2(k_x, k_z)$ ,  $\|\mathcal{H}_v\|_2(k_x, k_z)$ ,  $\|\mathcal{H}_w\|_2(k_x, k_z)$  in Poiseuille flow with  $Re = 2000$ .

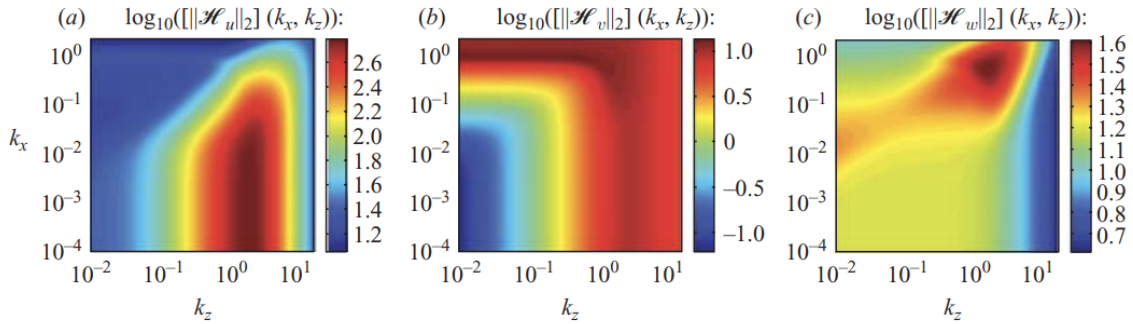


Figure 6: Plots of  $\|\mathcal{H}_u\|_2(k_x, k_z)$ ,  $\|\mathcal{H}_v\|_2(k_x, k_z)$ ,  $\|\mathcal{H}_w\|_2(k_x, k_z)$  in Poiseuille flow with  $Re = 2000$ , Reprinted from Fig. 4, in Jovanović and Bamieh, 2005b.

$\mathcal{H}_2$  norms from forcing to the components of the fluid's velocity field are illustrated in figure 5. figure 6 shows same plot but taken from Jovanović and Bamieh, 2005b. One can see that we accurately reproduce these plots with our solver. The strongest mode of amplification in  $v$  is achieved when  $k_x \approx O(1)$ ,  $k_z = 0$  and has a magnitude in the order of  $O(10)$ , which is the weakest among the velocity components amplifications. The strongest mode of amplification of  $u$  is when  $k_x = 0$  and  $k_z \approx O(1)$  and the strongest mode of amplification in  $w$  is the TS mode, meaning  $k_x \approx O(1)$  and  $k_z \approx O(1)$ . Overall, the pairs of  $\|\mathcal{H}_w\|_2$ ,  $\|\mathcal{H}_x\|_2$  and  $\|\mathcal{H}_u\|_2$ ,  $\|\mathcal{H}_z\|_2$  are similar in their behavior.

Lastly, we show as illustrated in figure 7, the  $\|\mathcal{H}\|_2$ , which represents the energy of all velocity components due to forcing from all 3 components. One can see a great agreement comparing it with figure 8 that we reproduced from Jovanović and Bamieh, 2005b. As expected, the dominant wave numbers correspond to streamwise components due to perpendicular forcing.

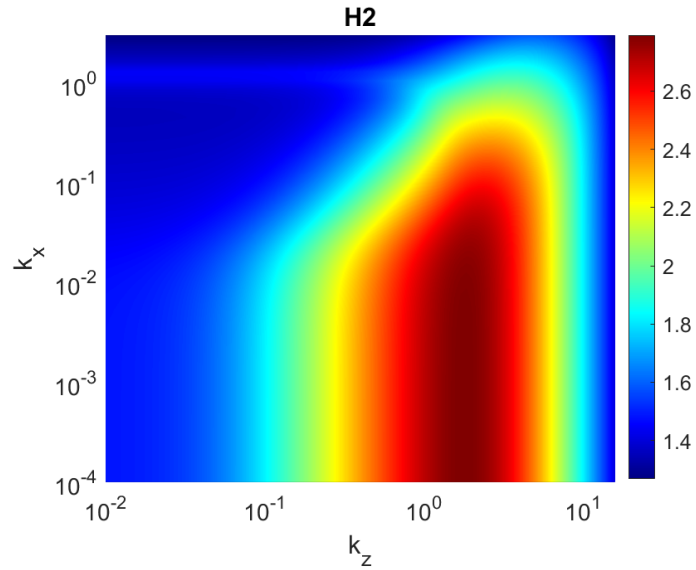


Figure 7: Plot of  $\|\mathcal{H}\|_2(k_x, k_z)$  in Poiseuille flow with  $Re = 2000$ .

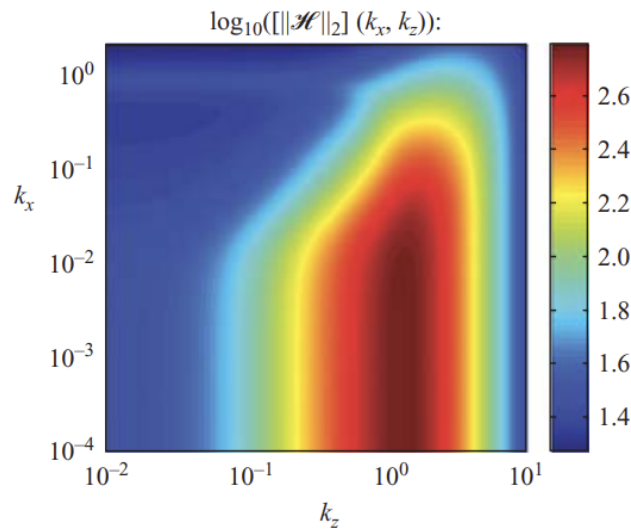


Figure 8: Plot of  $\|\mathcal{H}\|_2(k_x, k_z)$  in Poiseuille flow with  $Re = 2000$ , Reprinted from Fig. 5, Jovanović and Bamieh, 2005b.

The plot of the most encompassing  $\mathcal{H}_2$  norm demonstrates mainly that the mode with the largest amplification, representing the amplification of kinetic energy of the fluid, is the mode of spacing in the  $z$ -direction only, maintaining the relation  $k_x = 0$  and  $k_z \approx O(1)$ . As one can see, the results obtained throughout this entire section are identical to the results in Jovanović and Bamieh, 2005b, validating the model used and allowing us to use it for making different predictions.

### 3.1.2 Blasius flow

In this section we show results of application our input-output LNS solver to laminar Blasius base flow profile, which was obtained numerically by solving the Blasius equation:  $2f''' + ff'' = 0$ , where  $f$  is the normalized base flow velocity varying with a function of the similarity thickness variable  $\eta = y/\delta^*$ , where  $\delta^*$  is a displacement thickness. To compute all the  $\mathcal{H}_2$  norms, equation 24 was solved numerically using  $N = 40$  Chebyshev points in wall normal direction, whereas for the horizontal wave-number domain, same grid of  $(k_x, k_z)$  values was used as for the Poiseuille flow case.

In figures 9-13, all types of norms are calculated for the Reynolds number of  $Re = 530$ . This value for the Reynolds number was used for the modeling of the plasma actuator array in Belson et al., 2012 and Gluzman and Gayme, 2021b. The obtained  $\|\mathcal{H}_{rs}(k_x, k_z)\|$  norms, where  $r = \{u, v, w\}$  and  $s = \{x, y, z\}$ , are illustrated in figure 9. These norms represent amplification of single velocity component by a single forcing components. All results are presented on a logarithmic scale.

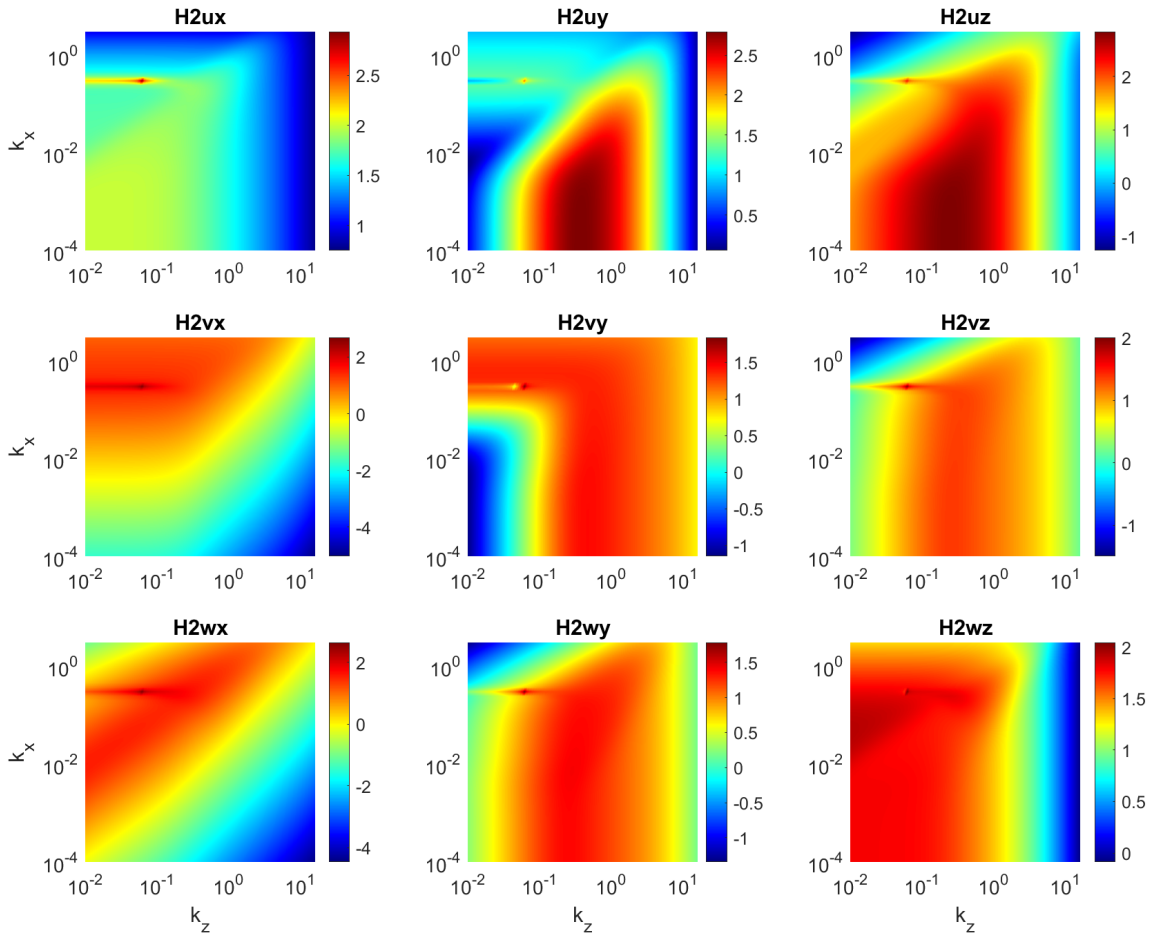


Figure 9: Plots of  $\|\mathcal{H}_{rs}\|_2(k_x, k_z)$  in Blasius flow with  $Re = 530$ .

All norms have a similar general structure to the ones produced in Poiseuille flow, but there are some key differences between them. The most obvious difference is the presence of a localized region of high amplification in all plots, at wave lengths of  $k_x \approx 10^{-1}$  and  $k_z \approx 10^{-1}$ . This wave-number pair correspond to an oblique wave mode, propagating at 45

degrees to the free stream. Generally, all  $\mathcal{H}_2$  norms reach higher peaks in Blasius base flow than in Poiseuille base flow, demonstrating that Blasius flow serve as a stronger amplifier to disturbances than Poiseuille flow.

This statement is merely based on the observed amplification ranges of the disturbance, as shown in the color bar for each plot, and requires some clarifications as we consider different geometries with different boundary conditions and Reynolds numbers. In particular, the Reynolds number over a flat plate is defined as:

$$Re = \frac{U\delta^*}{\nu}, \quad (32)$$

where  $\delta^*$  is the displacement thickness and  $\nu$  is the kinematic viscosity. For Poiseuille base flow in a channel of height  $H$  between the top and bottom walls, the displacement thickness is  $\delta^* = \frac{H}{6}$  while for Blasius base flow  $\delta^* = 1.72\sqrt{\frac{\nu x}{U}}$ , where  $U$  is the velocity of the flow above the plate and  $x$  is the streamwise direction coordinate. Moreover, the Reynolds number is defined at the location of the actuation, and any increase of Reynolds number corresponds in increase of velocity.

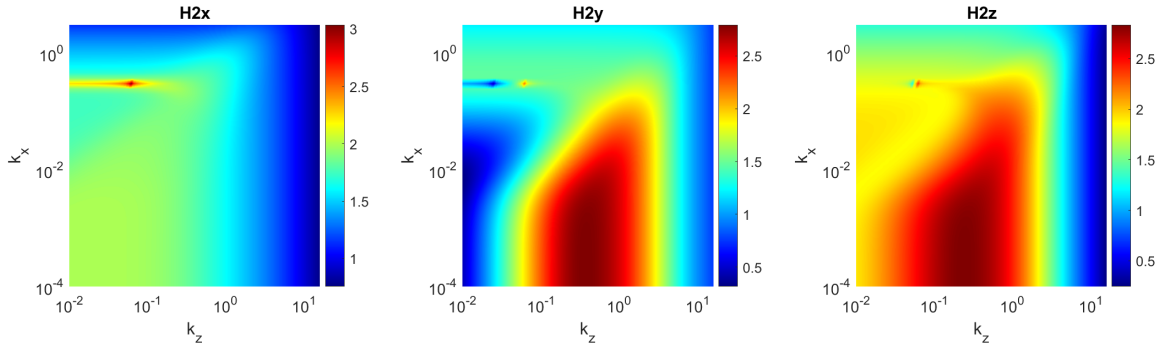


Figure 10: Plots of  $\|\mathcal{H}_x\|_2(k_x, k_z)$ ,  $\|\mathcal{H}_y\|_2(k_x, k_z)$ ,  $\|\mathcal{H}_z\|_2(k_x, k_z)$  in Blasius flow with  $Re = 530$ .

Energy amplification of each forcing direction is illustrated in figure 10.  $\|\mathcal{H}_y\|_2$  and  $\|\mathcal{H}_z\|_2$  are similar to the same norms in Poiseuille flow and both has their biggest magnitude when  $k_x = 0$  and  $k_z \approx O(1)$ . They differ from the Poiseuille case by the specific wave number in the  $z$  direction for maximal amplification, which in this case is lower.  $\|\mathcal{H}_x\|_2$  appears visually to be very different but has the same structure as in the Poiseuille case (figure 3). The visual difference stems from the localized point of high amplification in the  $(k_x, k_z)$  domain, which corresponds to an oblique wave mode that is shown also in figure 9. For the  $\mathcal{H}_x$  sub-operator this mode is an order of magnitude stronger than any other wave lengths combinations on the same plot, where the amplification value at the localized point is  $\|\mathcal{H}_x\|_2 \approx 10^3$  while the largest value for any other wave number combination is  $\|\mathcal{H}_x\|_2 \approx 10^2$ . This localized point of amplification can be found also in the plots of  $\|\mathcal{H}_y\|_2$  and  $\|\mathcal{H}_z\|_2$  but with weaker magnitudes such that it doesn't distort the whole image and the strongest mode of amplification is the streaks mode.

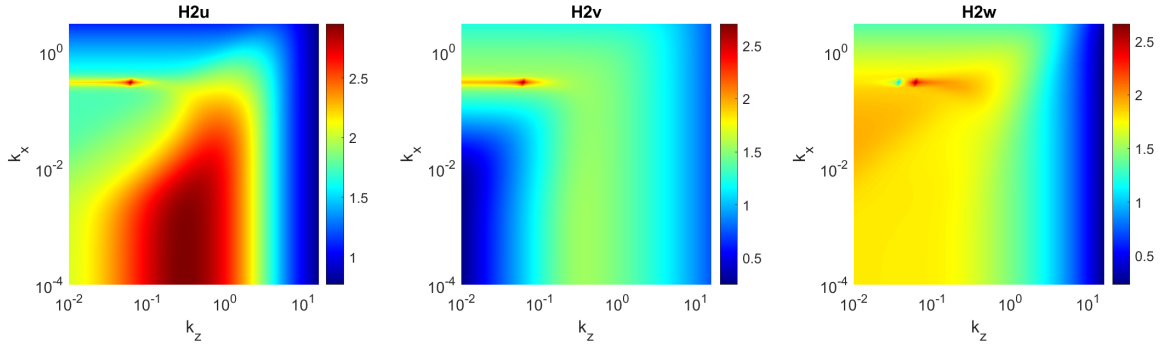


Figure 11: Plots of  $\|\mathcal{H}_u\|_2(k_x, k_z)$ ,  $\|\mathcal{H}_v\|_2(k_x, k_z)$ ,  $\|\mathcal{H}_w\|_2(k_x, k_z)$  in Blasius flow with  $Re = 530$ .

The  $\mathcal{H}_2$  norms from forcing to the components of the fluid's velocity field are illustrated in figure 11. The region of sudden peak in amplification is apparent in all the velocity sub operators.  $\|\mathcal{H}_u\|_2$  has 2 dominant modes of amplification with similar magnitudes. These modes being the oblique wave mode with wave numbers  $k_x \approx 10^{-1}$  and  $k_z \approx 10^{-1}$  and the streaks mode with wave numbers  $k_x = 0$  and some value  $k_z \approx O(1)$ . In contrast,  $\|\mathcal{H}_v\|_2$  and  $\|\mathcal{H}_w\|_2$  has an obvious maximum in the oblique wave mode, similarly to  $\|\mathcal{H}_x\|_2$ . The full  $\|\mathcal{H}\|_2$  from forcing to reaction is illustrated in figure 12.

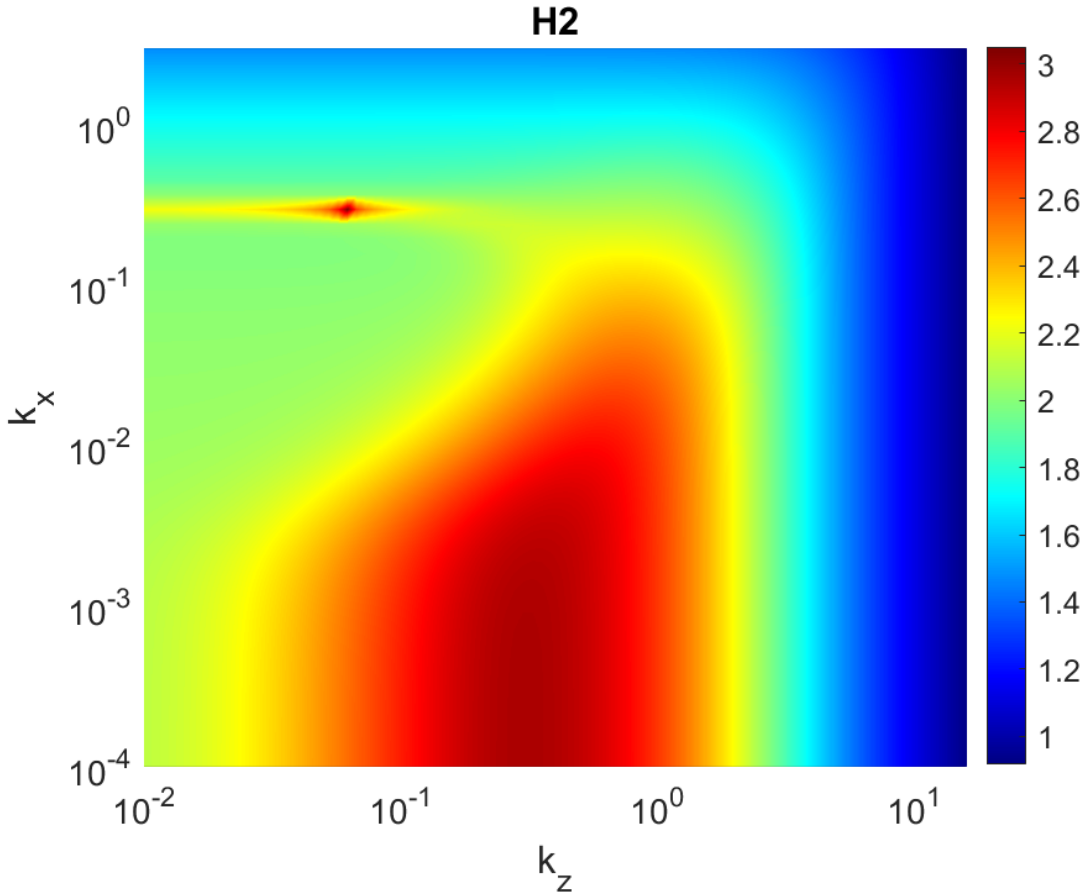


Figure 12: Plot of  $\|\mathcal{H}\|_2(k_x, k_z)$  in Blasius flow with  $Re = 530$ .

This  $\|\mathcal{H}\|_2$  norm is very similar to the one obtained for Poiseuille base flow. It has strong streaks mode with wave numbers of  $k_x = 0$  and some value of  $k_z \approx O(1)$  and decays continuously for other pairs of wave numbers. The main area of difference is the new oblique wave mode which has a slightly higher magnitude than the streaks mode.

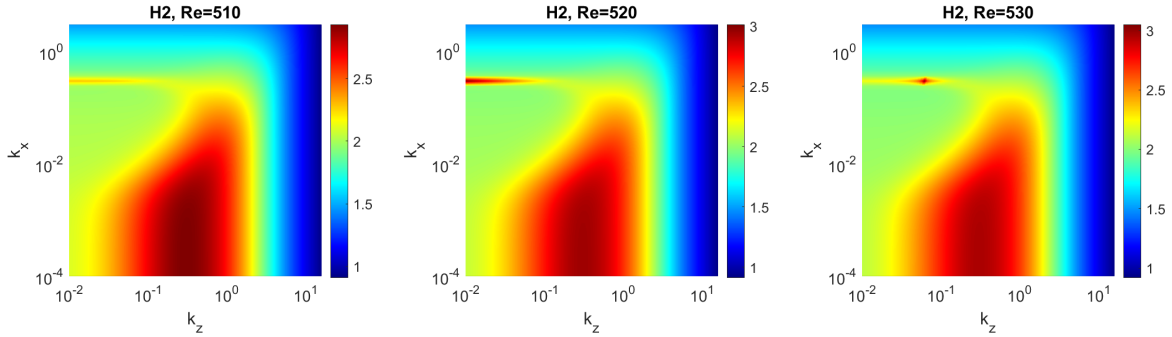


Figure 13: Plots of  $\|\mathcal{H}\|_2(k_x, k_z)$  in Blasius flow with  $Re = 510$ ,  $Re = 520$  and  $Re = 530$ .

The oblique wave mode is highly dependent on the Reynolds number, as can be seen in figure 13. The spanwise wave number of the oblique wave mode increases when increasing the Reynolds number. At  $Re = 520$  the spanwise wave number of this mode is  $k_z \approx O(10^{-2})$ , making it more similar to a TS wave mode. At  $Re = 510$  this mode is not evident, and the strongest mode of amplification is the streaks mode that cannot be captured by stability theory, that only predicts single 2D TS mode as least stable mode for the critical Reynolds number of  $Re_{cr} = 520$  for Blasius boundary layer (Jordinson, 1970). However, our analysis captures both the least stable 2D mode that predicted from linear flow stability analysis (Schmid et al., 2002) and more dominant streaky structure that associated to bypass transition scenarios and observed in experimental studies. We note that the mentioned amplification mode stays an oblique mode and keep being localized around similar wave numbers when increasing the Reynolds number, as demonstrated in figure 14:

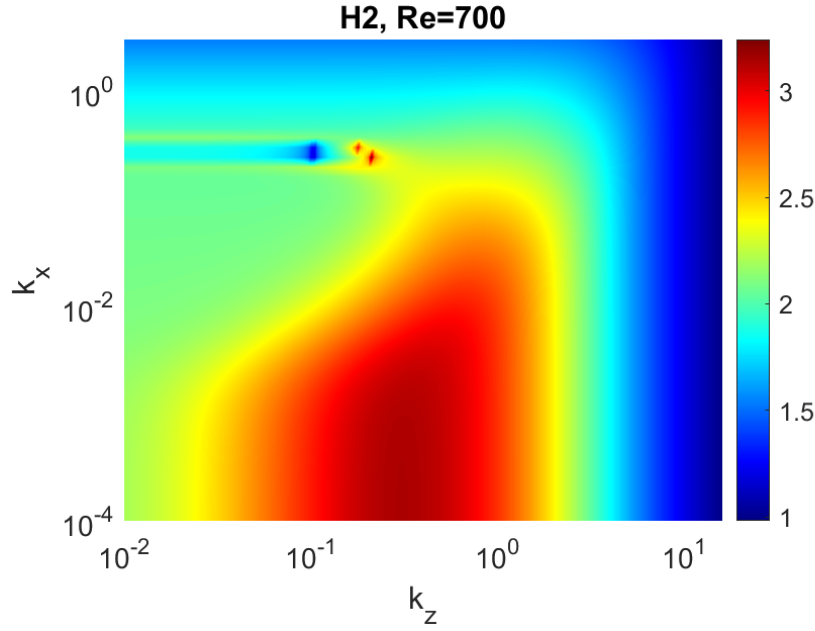


Figure 14: Plot of  $\|\mathcal{H}\|_2(k_x, k_z)$  in Blasius flow with  $Re = 700$ .

### 3.2 Line Actuator Response

In this section, we use our input-output solver to reproduce the flow response to spanwise array of symmetric DBD plasma actuators setup that studied in Hanson et al., 2010 and Belson et al., 2012. The mentioned setup is presented in figure 15. The body forcing from electrode edges is modeled by 4 strips, where 2 creating forcing in the positive  $z$  direction (indicated by magenta) and 2 creating forcing in the negative  $z$  direction (indicated by cyan), similarly to the work done in Gluzman and Gayme, 2021b and demonstrated in figure 16. Each strip is modeled by a cluster of point sources of localized forcing. The spacing between point sources is 0.1 non-dimensional units, where the non-dimensional units are normalized by the displacement thickness  $\delta^*$ . We verify that the selected spacing length is sufficiently small by doubling the number of sources and verifying that the changes to the results are negligible. In this case, the chosen Reynolds number is  $Re = U\delta^*/\nu = 530$ , which corresponds to  $\delta^* = 1.59[mm]$ , for a free stream velocity of  $U = 5[m/s]$ . The spacing between each plasma actuator is  $\Delta z = 20[mm]$  and length of each actuator is  $l = 40[mm]$  and thus we use 252-point sources of localized forcing.

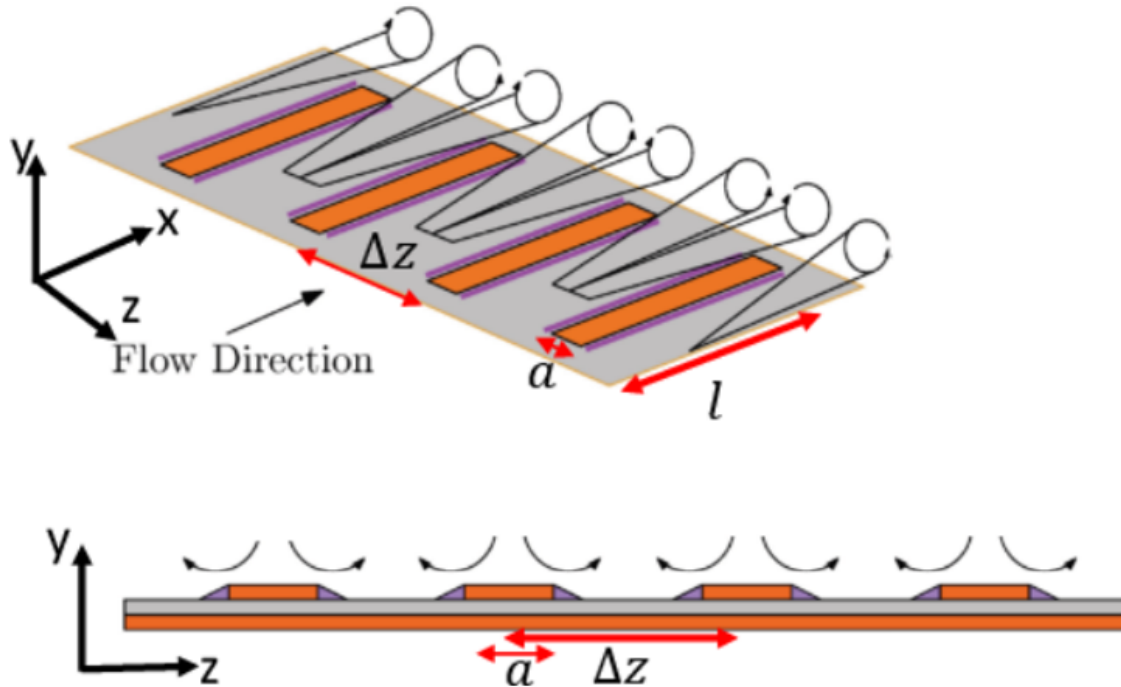


Figure 15: Spanwise array of DBD plasma actuators. Figure reproduced from Gluzman and Gayme, 2021b.

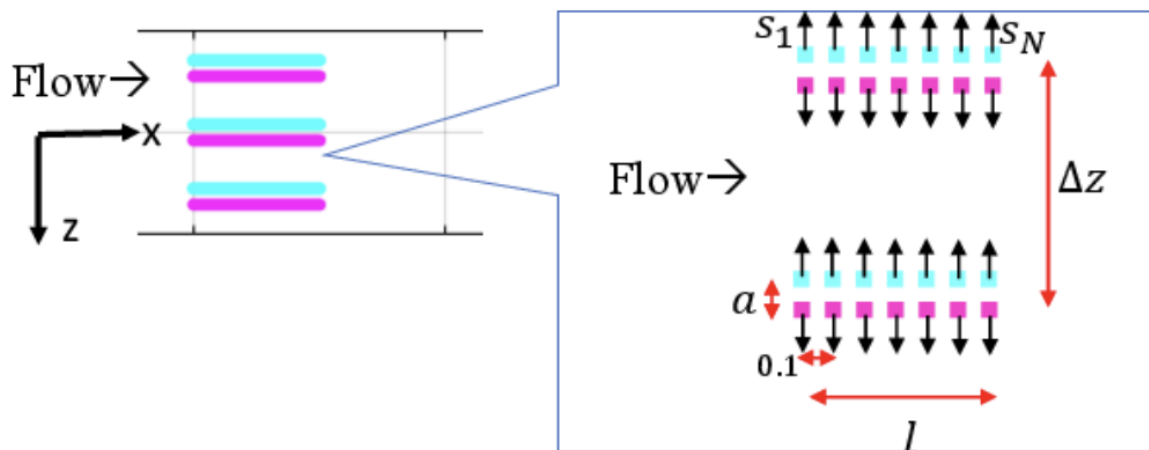


Figure 16: Forcing Setup used to simulate plasma actuators response. Figure reproduced from Gluzman and Gayme, 2021b.

Before testing the flow response for the array of plasma actuators, the impulse response of the model was checked and validated with results from M. R. Jovanovic, 2004, which detail in Appendix B. The temporal forcing input chosen for the plasma actuator array is a unit step function, applied to each point source in the setup shown in figure 16. The solution for the flow field in the steady state was calculated using Eq. (29).

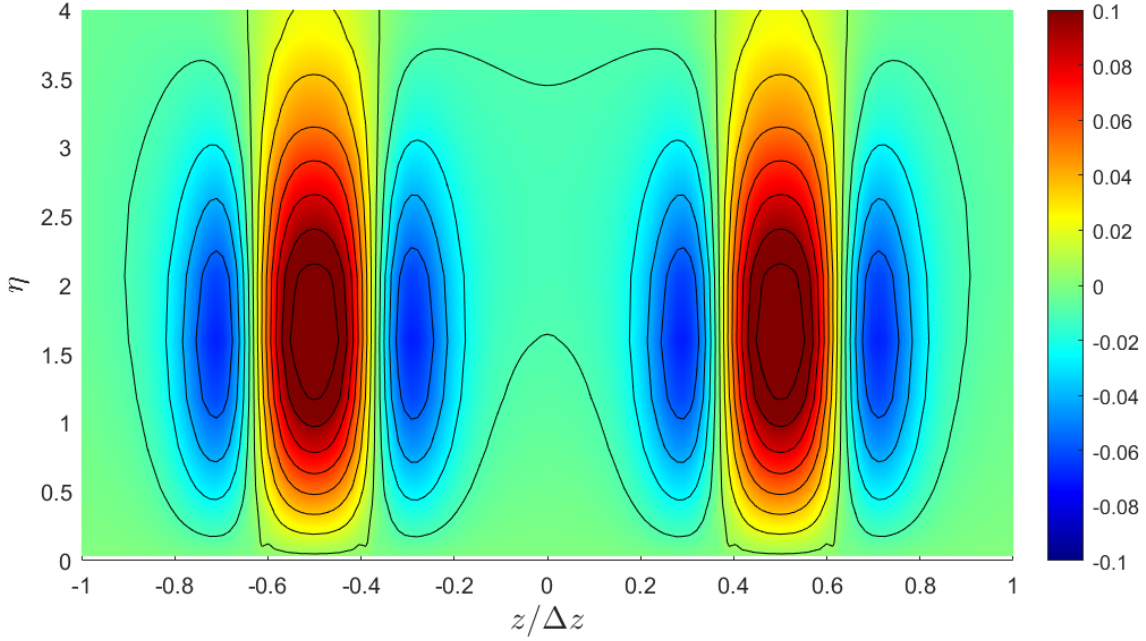


Figure 17: Normalized perturbation stream-wise velocity at a particular stream-wise location (a  $y - z$  plane)  $200[mm]$  downstream of an array of plasma actuators. Here  $\eta = y(U/\nu x)^{1/2}$  is the Blasius length scale, where  $\nu$  is the kinematic viscosity,  $y$  is the wall-normal distance,  $U$  is the free-stream stream-wise velocity, and  $x$  is the stream-wise distance from the leading edge. The variable  $z$  is the stream-wise distance from the center of the domain and  $\Delta z$  is the spacing between actuator pairs.

A  $y$ - $z$  cross section of the normalized streamwise component of the perturbation velocity at  $x = 200[mm]$  downstream the actuator array is shown in figure 17. This specific location was chosen for validating the results with Belson et al., 2012 and Gluzman and Gayme, 2021b. Figure 17 demonstrate that our model obtains good qualitative agreement in terms of the shape of the flow structures with both DNS simulations (Belson et al., 2012) and with the previous work of Gluzman and Gayme, 2021b. The streaks of streamwise velocity follow the positioning of the actuator electrodes in the array, with low-momentum regions between the electrode pairs.

### 3.3 Optimal Actuator Arrangement for Maximal response

The idea in this section is to find the optimal spacing between electrodes of spanwise array symmetric plasma actuator that presented in Section 3.2 for maximal response of the streamwise velocity component amplification. We utilize in our analysis the approach used in Section 3.1.2 to obtain energy amplification of different wave number pairs for predicting the spanwise spacing  $\Delta z$  between the actuator electrodes, that produces the maximal amplification. As seen in figure 9, the maximal value of  $\mathcal{H}_{uz}$  is reached when  $k_x = 0$ . Thus, we focus only on spacing along the  $z$  direction. We quantify the amplitude of the response for different spacing lengths between the actuators using the following equation:

$$A(\Delta z) \equiv \frac{1}{Re^4} \int \int \int u^2(\Delta z) dx dy dz. \quad (33)$$

Here,  $\Delta z$  is the spacing between the 2 actuators and  $u^2$  represents the kinetic energy density of the perturbation velocity in the streamwise direction.

We examine relationship between the amplitude of energy perturbations for different Reynolds numbers. As mentioned before the Reynolds number is defined as  $Re = U\delta^*/\nu$ , where  $\delta^*$  is the displacement thickness and  $\nu$  is the kinematic viscosity. The displacement thickness remains constant under the assumption of parallel boundary layer and we assume  $\nu$  to be constant as well. Thus, changing the Reynolds number is equivalent to changing the base flow velocity  $U$ .

The specific definition of the amplitude in Eq. (33) is chosen with the goal of comparing the behavior of the actuator array subjected to base flows with different Reynolds numbers. In Jovanović and Bamieh, 2005b, it is shown that for  $k_x = 0$ , the norm  $\|\mathcal{H}_{uz}\|_2^2$  scales with  $Re^3$ . However, we need to account for the fact that the integration in Eq. (33) is done also in the  $y$  direction. As mentioned in section 2,  $\mathcal{H}_{uz}$  changes its value for every point along the  $y$  direction. Because the Reynolds number is proportional to the length scale of the problem, we divide by it once more to account for the integration in the  $y$  direction, leaving us with a coefficient of  $1/Re^4$  in Eq. (33). If the model in section 2 holds completely for the case of actuator array, we would expect that  $A(\Delta z)$  would be independent of the Reynolds number. To check this hypothesis, we define a wave number matching every spacing length in the following way:

$$k_{\Delta z} \equiv \frac{2\pi}{\Delta z}. \quad (34)$$

The amplitude of energy perturbation of the flow was calculated for  $k_{\Delta z} \in [0.2, 1]$ . The results for  $Re = 200$  and  $Re = 530$  is presented in figure 18:

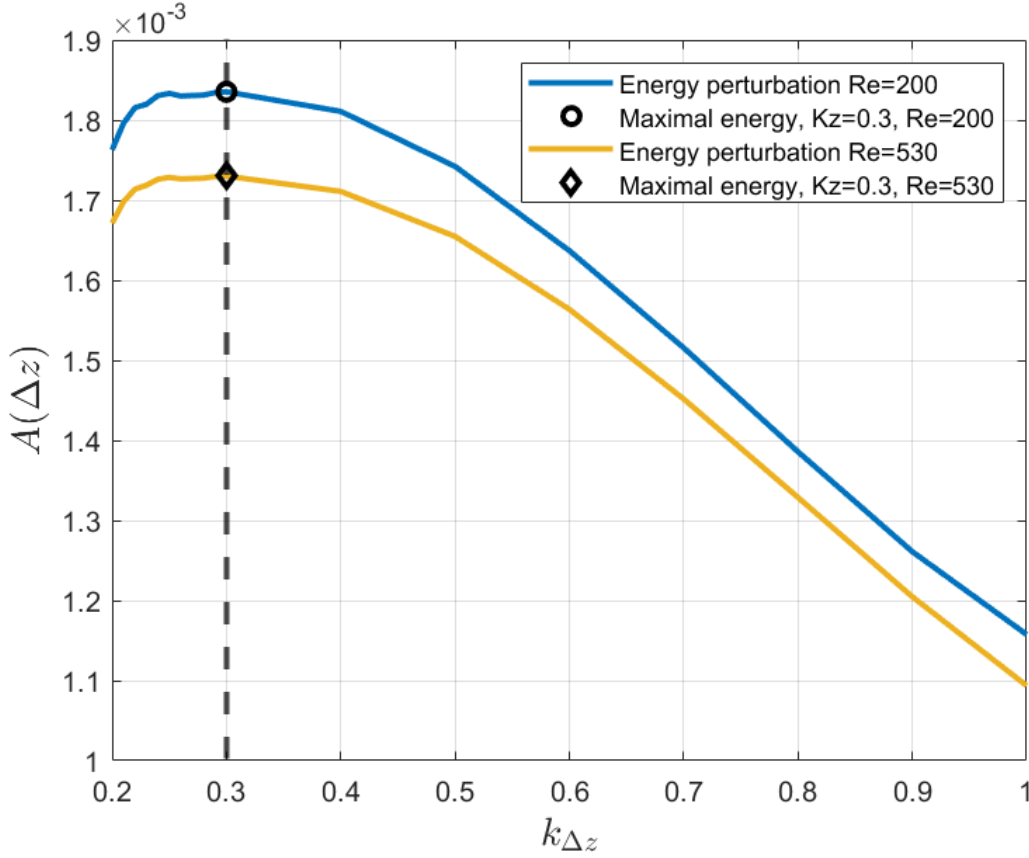


Figure 18: Streamwise kinetic energy perturbation for changing actuator spacing with  $Re = 200$  and  $Re = 530$ .

This graph was obtained by solving Eq. (29) for different wave numbers that correspond to different spacings between actuators with the relation in Eq. (34). We note that both graphs have a peak at a wave number of  $k_z = 0.3$ , making it the optimal wave number for maximal kinetic energy perturbation regardless of the Reynolds number. In addition, the difference between the graphs for different Reynolds numbers is small. This means that while there is some dependence on the Reynolds number, the behavior of the flow over the actuator array is similar to the behavior of flow with some harmonic forcing. Our next objective is to try to find an analogous harmonic forcing that would behave similarly to the flow field around the actuator array.

As seen in figure 16, the setup has 4 strips that create forcing. The 2 outer strips create forcing in opposing directions, as the 2 inner ones. Thus, we can use this fact to approximate the forcing term as a combination of 2 sine waves. This approach is demonstrated in figure 19:

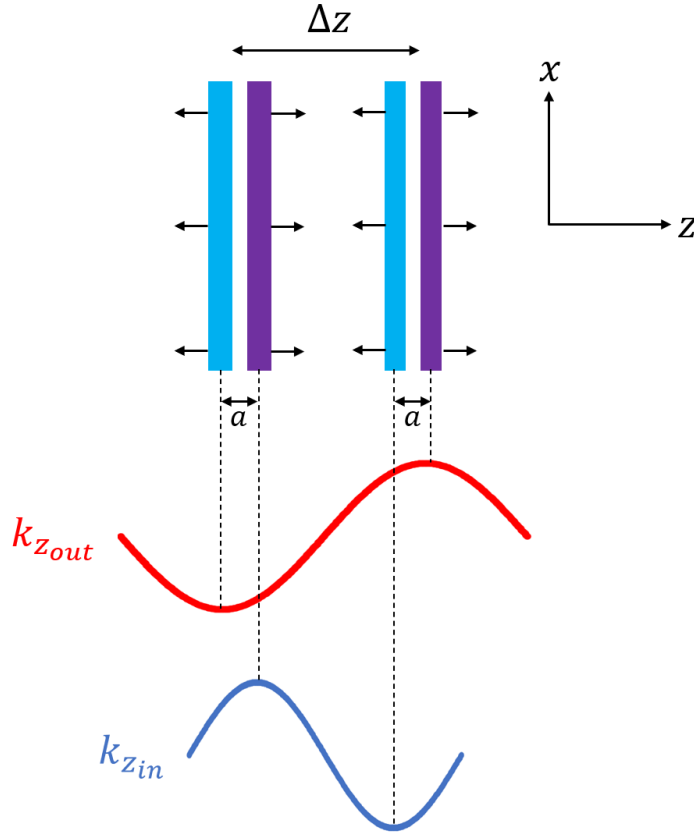


Figure 19: assigning wave numbers to the experimental setup

Using the geometry of the problem we get:

$$k_{z_{out}} = \frac{\pi}{\Delta z} + a = \frac{1}{2}k_{\Delta z} + a, \quad (35)$$

$$k_{z_{in}} = \frac{\pi}{\Delta z} - a = \frac{1}{2}k_{\Delta z} - a.$$

To predict the wave number for maximal response we propose we to approximate the forcing term  $d$  as the sum of the 2 sine waves in figure 19:

$$\mathbf{d}_{combined} = [0, 0, \sin(k_{z_{out}}z) + \sin(k_{z_{in}}z)]^T. \quad (36)$$

Using Eq. (10) and the forcing term in Eq. (36), the solution to Eq. (2) is:

$$\phi = \mathcal{H}_z(0, k_{z_{in}}) \sin(k_{z_{in}}z) + \mathcal{H}_z(0, k_{z_{out}}) \sin(k_{z_{out}}z). \quad (37)$$

This fact is true due to the linear nature of Eq. (2). To get the amplification for the streamwise velocity component, we can use the decomposition of the  $\mathcal{H}$  operator presented in Eq. (12):

$$u = \mathcal{H}_{uz}(0, k_{z_{in}}) \sin(k_{z_{in}}z) + \mathcal{H}_{uz}(0, k_{z_{out}}) \sin(k_{z_{out}}z). \quad (38)$$

Using Eq. (38), We can approximate the amplification with the following expression:

$$\|\mathcal{H}_{uz}^{combined}\|_2^2 = \|\mathcal{H}_{uz}(0, k_{z_{in}})\|_2^2 + \|\mathcal{H}_{uz}(0, k_{z_{out}})\|_2^2. \quad (39)$$

As mentioned before, the quantity  $\|\mathcal{H}_{uz}(0, k_z)\|_2^2$  is proportional to  $Re^3$ . Hence, the quantities  $\frac{1}{Re^3}\|\mathcal{H}_{uz}(0, k_z)\|_2^2$ ,  $\|\mathcal{H}_{uz}^{combined}\|_2^2$  are not dependent on the Reynolds number and represent the behavior of the system in a more general sense. Plots of  $\frac{1}{Re^3}\|\mathcal{H}_{uz}^{combined}\|_2^2$  and  $\frac{1}{Re^3}\|\mathcal{H}_{uz}\|_2^2$  for different wave numbers in the spanwise direction are presented in figure 20:

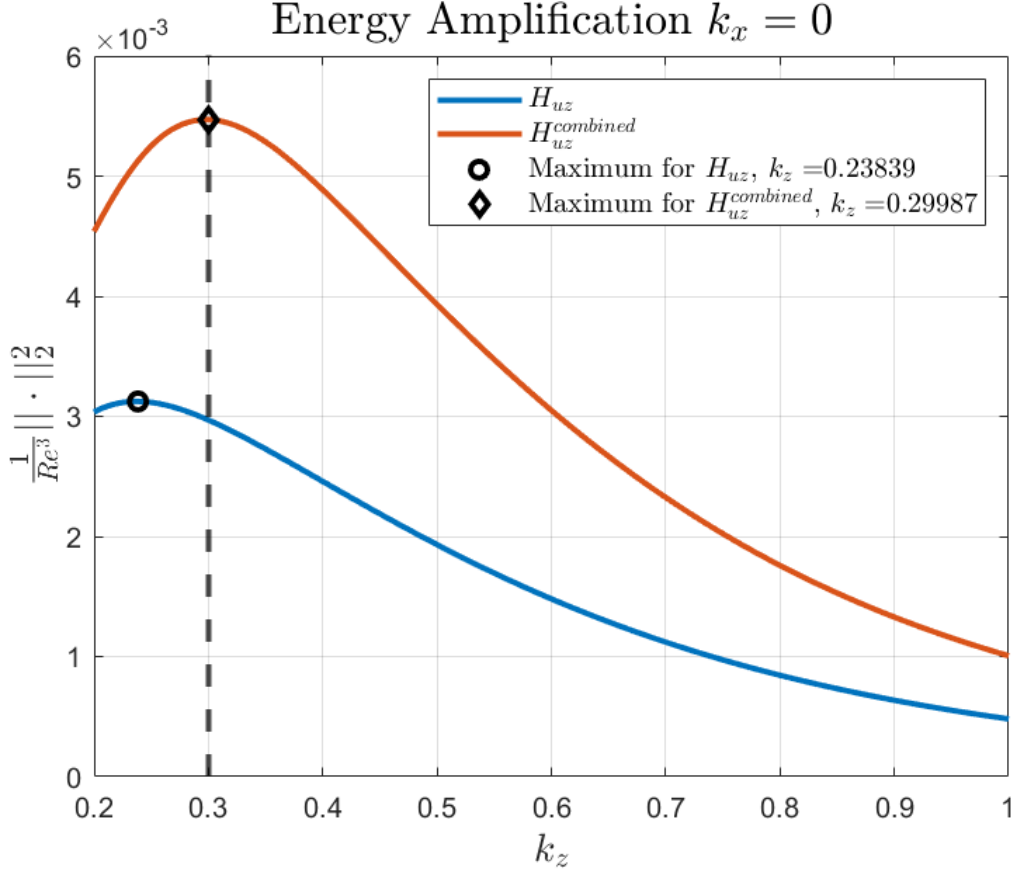


Figure 20: Plots of  $\frac{1}{Re^3}\|\mathcal{H}_{uz}^{combined}\|_2^2$  and  $\frac{1}{Re^3}\|\mathcal{H}_{uz}(k_x = 0, k_z)\|_2^2$  for Blasius base flow, both computed at  $Re = 530$ .

Considering the results from figure 18, the  $\mathcal{H}_{uz}^{combined}$  norm predicts the optimal wave number for maximal amplification correctly at  $k_z \approx 0.3$ , when the regular  $\mathcal{H}_{uz}$  norm has its peak at  $k_z \approx 0.24$ , not the optimal wave number to set the actuator's electors spanwise spacing. Hence, it is evident that the process of identifying two wave numbers that are relevant to the problem yields better results than considering only one wave number. The results were obtained by calculating  $\|\mathcal{H}_{uz}\|_2^2$  using Eq. (15) and by adding up the values for the corresponding wave numbers as described in Eq. (39). As mentioned previously, this graph is independent of the choice of the Reynolds number and thus, the wave number for maximal energy is the same for all Reynolds numbers if neglecting the non-parallel effects of boundary layer growths. We note that the combined time that took to calculate all the results for figure 18 using Eqs (31) is 38 hours in regular laptop, while with our novel approach, using Eq. (39), the calculation took about 2 minutes to obtain the result in figure 20, i.e., at significant reduction of computational time of the order of  $O(10^3)$ .

## 4 Conclusions

In this project, an LNS input-output solver was developed to study high-dimensional actuated boundary layer systems subject to external forcing, which are of high relevance to active flow control applications and actuator design. In particular, the externally forced linearized Navier-Stokes (LNS) equations system has been used to examine the important dynamic processes, structural features, and energy pathways of transitional wall-bounded shear flows. First, we validated our LNS input-output solver with results from the literature by reproducing the amplification of the kinetic energy density norms of each velocity component in channel flow for different forcing directions.

Second, we used our solver to study the flow physics of energy amplification subject to external periodic forcing for the Blasius boundary layer. We find that all norms have a similar general structure to the ones produced in Poiseuille flow, but there are some key differences between them. The most obvious difference is the presence of an oblique wave mode, propagating at 45 degrees to the free stream. Generally, all energy norms reach higher peaks in Blasius base flow than in Poiseuille base flow, demonstrating that Blasius flow serves as a stronger amplifier to disturbances than Poiseuille flow.

Third, we extended our input-output solver to model the flow response to actuation following Gluzman and Gayme, 2021a approach and validated the method via reproducing the flow response to a spanwise array of symmetric DBD plasma actuators setup studied in Hanson et al., 2010 and Belson et al., 2012.

Lastly, we propose a simplified novel approach with our input-output solver to study the flow response to the spanwise plasma actuator array. A single wave number pair is used to determine the optimal wave number combination for achieving maximal amplification of streamwise velocity perturbations. This approach can determine the optimized spanwise spacing of the plasma actuator array in a fraction of the time that it takes with a regular input-output approach of Gluzman and Gayme, 2021b. However, our approach is limited to steady-state periodic forcing in time and space; hence, it is limited to only certain sets of actuators with spanwise periodic geometry and for parallel shear flows. Our future work will focus on generalizing the method for optimizing actuators with non-period spatial-temporal forcing depending on the framework to be applied for nonparallel pressure-driven boundary layers over curved geometries, such as airfoils, and conduct experimental studies to validate the modeling effort.

## A Appendix: Input-output model derivation

To write Eq. (1) in a state-space form, we start by writing it explicitly, rather than in a vector representation:

$$\begin{cases} \frac{\partial u}{\partial t} = -U \frac{\partial u}{\partial x} - U'v - \frac{\partial p}{\partial x} + \frac{1}{Re} \nabla^2 u + d_x, \\ \frac{\partial v}{\partial t} = -U \frac{\partial v}{\partial x} - \frac{\partial p}{\partial y} + \frac{1}{Re} \nabla^2 v + d_y, \\ \frac{\partial w}{\partial t} = -U \frac{\partial w}{\partial x} - \frac{\partial p}{\partial z} + \frac{1}{Re} \nabla^2 w + d_z, \\ \frac{\partial u}{\partial x} + \frac{\partial v}{\partial y} + \frac{\partial w}{\partial z} = 0. \end{cases} \quad (\text{A1})$$

We can take the Laplacian of the equation for  $v$  and get:

$$\nabla^2 \frac{\partial v}{\partial t} = -\nabla^2 U \frac{\partial v}{\partial x} - U \nabla^2 \left( \frac{\partial v}{\partial x} \right) - \nabla^2 \left( \frac{\partial p}{\partial y} \right) + \frac{1}{Re} \nabla^4 v + \nabla^2 d_y. \quad (\text{A2})$$

We can rearrange the LHS, considering that the base profile  $U$  is dependent only on  $y$ :

$$\nabla^2 \frac{\partial v}{\partial t} = -U'' \frac{\partial v}{\partial x} - U \frac{\partial}{\partial x} (\nabla^2 v) - \frac{\partial}{\partial y} (\nabla^2 p) + \frac{1}{Re} \nabla^4 v + \nabla^2 d_y. \quad (\text{A3})$$

An expression to the pressure gradient can be obtained using Eq. (A1):

$$\nabla p = -\frac{\partial \mathbf{u}}{\partial t} - U \frac{\partial \mathbf{u}}{\partial x} - \begin{bmatrix} U'v \\ 0 \\ 0 \end{bmatrix} + \frac{1}{Re} \nabla^2 \mathbf{u} + \mathbf{d}. \quad (\text{A4})$$

Here, a bold symbol indicates a vector variable. By applying the divergence operator to Eq. (A4), we get an expression to the Laplacian of the pressure which we can later substitute into Eq. (A3).

$$\nabla^2 p = -\frac{\partial}{\partial t} (\nabla \cdot \mathbf{u}) - \nabla \cdot \left( U \frac{\partial \mathbf{u}}{\partial x} \right) - \nabla \cdot \begin{bmatrix} (U'v) \\ 0 \\ 0 \end{bmatrix} + \frac{1}{Re} \nabla^2 (\nabla \cdot \mathbf{u}) + \nabla \cdot \mathbf{d}. \quad (\text{A5})$$

From incomprehensibility,  $\nabla \cdot \mathbf{u} = 0$ . Further simplifying the LHS:

$$\nabla \cdot \left( U \frac{\partial \mathbf{u}}{\partial x} \right) = U \frac{\partial}{\partial x} (\nabla \cdot \mathbf{u}) + U' \frac{\partial v}{\partial x} = U' \frac{\partial v}{\partial x}, \quad (\text{A6})$$

$$\nabla \cdot \begin{bmatrix} (U'v) \\ 0 \\ 0 \end{bmatrix} = U' \frac{\partial v}{\partial x}. \quad (\text{A7})$$

Substituting A6 and A7 into A5, we get:

$$\nabla^2 p = -2U' \frac{\partial v}{\partial x} + \frac{\partial d_x}{\partial x} + \frac{\partial d_y}{\partial y} + \frac{\partial d_z}{\partial z}. \quad (\text{A8})$$

Now that we have an expression for the pressure gradient, we can plug it into Eq. (A3) while neglecting second order terms:

$$\nabla^2 \frac{\partial v}{\partial t} = -U'' \frac{\partial v}{\partial x} - U \frac{\partial}{\partial x} (\nabla^2 v) + 2U'' \frac{\partial v}{\partial x} + \frac{1}{Re} \nabla^4 v - \frac{\partial^2 d_x}{\partial x \partial y} - \frac{\partial^2 d_y}{\partial y^2} - \frac{\partial^2 d_z}{\partial y \partial z} + \nabla^2 d_y. \quad (\text{A9})$$

We can further simplify the equation and get:

$$\nabla^2 \frac{\partial v}{\partial t} = U'' \frac{\partial v}{\partial x} - U \frac{\partial}{\partial x} (\nabla^2 v) + \frac{1}{Re} \nabla^4 v - \frac{\partial^2 d_x}{\partial x \partial y} - \frac{\partial^2 d_z}{\partial y \partial z} + \frac{\partial^2 d_x}{\partial x^2} + \frac{\partial^2 d_z}{\partial z^2}. \quad (\text{A10})$$

We obtained an equation containing only the base profile  $U$ , the wall normal velocity perturbation  $v$  and the forcing in different directions. This equation will be used later as the

first equation in the state-space representation, while the second equation depends on the wall normal component of the vorticity vector:

$$\omega_y = \frac{\partial u}{\partial z} - \frac{\partial w}{\partial x}. \quad (\text{A11})$$

Hence, if we take the partial derivative in the  $z$  direction of the equation for  $u$  in A1 and subtract from it the partial derivative in the  $x$  direction of the equation for  $w$  in A1 we will get an equation involving only  $\omega_y$  and  $v$ :

$$\frac{\partial \omega_y}{\partial t} = -U' \frac{\partial v}{\partial z} - U \frac{\partial \omega_y}{\partial x} + \frac{1}{Re} \nabla^2 \omega_y + \frac{\partial d_x}{\partial z} - \frac{\partial d_z}{\partial x}. \quad (\text{A12})$$

We now apply a double Fourier transform in the  $x$  and  $z$  directions to equations A10 and A12. The transform changes the domain of the problem from physical space to the wave number domain. In addition, under the transform the derivatives in the  $x$  and  $z$  directions are replaced with multiplication by  $ik_x$  and  $ik_z$  respectively, where  $i$  is the imaginary unit  $i = \sqrt{-1}$ .

$$\begin{cases} \hat{\Delta} \frac{\partial \hat{v}}{\partial t} = ik_x U'' \hat{v} - ik_x U \hat{\Delta} \hat{v} + \frac{1}{Re} \hat{\Delta}^2 \hat{v} - ik_x \frac{\partial \hat{d}_x}{\partial y} - ik_z \frac{\partial \hat{d}_z}{\partial y} - k_x^2 \hat{d}_x - k_z^2 \hat{d}_z, \\ \frac{\partial \hat{\omega}_y}{\partial t} = -ik_z U' \hat{v} - ik_x U \hat{\omega}_y + \frac{1}{Re} \hat{\Delta} \hat{\omega}_y + ik_z \hat{d}_x - ik_x \hat{d}_z. \end{cases} \quad (\text{A13})$$

The notation  $\hat{\square}$  is used to describe a transformed variable and  $\hat{\Delta} = \frac{\partial^2}{\partial y^2} - k_x^2 - k_z^2$  is the transformed Laplacian operator. From here on we omit the  $\hat{\square}$  symbol for convenience of notation. We Apply The inverse Laplacian to the equation for  $v$  in A13 and rewrite A13 in a matrix form:

$$\frac{\partial \boldsymbol{\psi}}{\partial t}(k_x, y, k_z, t) = [\mathcal{A}(k_x, k_z) \boldsymbol{\psi}(k_x, y, k_z, t)](y) + [\mathcal{B}(k_x, k_z) \mathbf{d}(k_x, k_z, t)](y), \quad (\text{A14})$$

where  $\boldsymbol{\psi} \equiv [v, \omega_y]^T$ . The operators denoted as  $\mathcal{A}$  and  $\mathcal{B}$  are defined below:

$$\mathcal{A} \equiv \begin{bmatrix} \mathcal{A}_{11} & 0 \\ \mathcal{A}_{21} & \mathcal{A}_{22} \end{bmatrix} \equiv \begin{bmatrix} -ik_x \Delta^{-1} U \Delta + ik_x \Delta^{-1} U'' + \frac{1}{Re} \Delta^{-1} \Delta^2 & 0 \\ -ik_z U' & -ik_x U + \frac{1}{Re} \Delta \end{bmatrix}, \quad (\text{A15})$$

$$\mathcal{B} \equiv [\mathcal{B}_x \quad \mathcal{B}_y \quad \mathcal{B}_z] \equiv \begin{bmatrix} \Delta^{-1} & 0 \\ 0 & I \end{bmatrix} \begin{bmatrix} -ik_x \frac{\partial}{\partial y} & -(k_x^2 + k_z^2) & -ik_z \frac{\partial}{\partial y} \\ ik_z & 0 & -ik_x \end{bmatrix}. \quad (\text{A16})$$

This concludes the derivation of the state equation. We choose the output of the system to be  $\boldsymbol{\phi} \equiv [u, v, w]^T$  to obtain the velocity perturbations field. The linearity of the system and the vorticity vector implies that the output equation is also linear and has the following form:

$$\boldsymbol{\phi}(k_x, y, k_z, t) = \mathcal{C}(k_x, k_z) \boldsymbol{\psi}(k_x, k_z, t)](y), \quad (\text{A17})$$

where  $\mathcal{C}$  is a  $3 \times 2$  matrix. Writing Eq. (A17) in an explicit form gives:

$$\begin{bmatrix} u \\ v \\ w \end{bmatrix} = \begin{bmatrix} \mathcal{C}_{11} & \mathcal{C}_{12} \\ \mathcal{C}_{21} & \mathcal{C}_{22} \\ \mathcal{C}_{31} & \mathcal{C}_{32} \end{bmatrix} \begin{bmatrix} v \\ \omega_y \end{bmatrix}. \quad (\text{A18})$$

We now want to find the components of  $\mathcal{C}$ . Looking at the second row of the matrix, it is obvious that  $\mathcal{C}_{21} = 1$ ,  $\mathcal{C}_{22} = 0$ . We can take the derivative in the  $x$  direction of the continuity equation (forth equation in A1) and get:

$$\frac{\partial^2 u}{\partial x^2} + \frac{\partial^2 v}{\partial x \partial y} + \frac{\partial^2 w}{\partial x \partial z} = 0. \quad (\text{A19})$$

By rearranging and adding the term  $\frac{\partial^2 u}{\partial z^2}$  to both sides we obtain the following equation:

$$\frac{\partial^2 u}{\partial x^2} + \frac{\partial^2 u}{\partial z^2} = -\frac{\partial^2 v}{\partial x \partial y} + \frac{\partial \omega_y}{\partial z}. \quad (\text{A20})$$

Now we apply a Fourier transform, turning the derivatives to constants in similar fashion to Eq. (A13):

$$-(k_x^2 + k_z^2)\hat{u} = -ik_x \frac{\partial \hat{v}}{\partial y} + ik_z \hat{\omega}_y, \quad (\text{A21})$$

thus, we know that the coefficients in the first row of the matrix  $\mathcal{C}$  are:

$$\mathcal{C}_{11} = \frac{ik_x \frac{\partial}{\partial y}}{k_x^2 + k_z^2}, \quad \mathcal{C}_{12} = -\frac{ik_z}{k_x^2 + k_z^2}. \quad (\text{A22})$$

A similar derivation can be done for  $\mathcal{C}_{31}$  and  $\mathcal{C}_{32}$ . Instead of differentiating the continuity equation in the  $x$  direction, we will differentiate in the  $z$  direction and obtain the following equation:

$$\frac{\partial^2 u}{\partial x \partial z} + \frac{\partial^2 v}{\partial y \partial z} + \frac{\partial^2 w}{\partial z^2} = 0. \quad (\text{A23})$$

Now we will add the term  $\frac{\partial^2 w}{\partial x^2}$  to both sides:

$$\frac{\partial^2 w}{\partial x^2} + \frac{\partial^2 w}{\partial z^2} = -\frac{\partial^2 v}{\partial y \partial z} - \frac{\partial \omega_y}{\partial x}. \quad (\text{A24})$$

Now, again, we apply a Fourier transform to obtain:

$$-(k_x^2 + k_z^2)\hat{w} = -ik_z \frac{\partial \hat{v}}{\partial y} - ik_x \hat{\omega}_y, \quad (\text{A25})$$

thus, we know that the coefficients in the third row of the matrix  $\mathcal{C}$  are:

$$\mathcal{C}_{31} = \frac{ik_z \frac{\partial}{\partial y}}{k_x^2 + k_z^2}, \quad \mathcal{C}_{32} = \frac{ik_x}{k_x^2 + k_z^2}. \quad (\text{A26})$$

We have calculated all the terms in  $\mathcal{C}$ , and hence it is given by the equation:

$$\mathcal{C} \equiv \begin{bmatrix} \mathcal{C}_u \\ \mathcal{C}_v \\ \mathcal{C}_w \end{bmatrix} \equiv \frac{1}{k_x^2 + k_z^2} \begin{bmatrix} ik_x \frac{\partial}{\partial y} & -ik_z \\ k_x^2 + k_z^2 & 0 \\ ik_z \frac{\partial}{\partial y} & ik_x \end{bmatrix}. \quad (\text{A27})$$

Equations A14, A15 and A16 describe the state equation of the state space while equations A17 and A27 describe the output equation. Hence, we obtained a full description of the state space form of the LNS equations.

## B Appendix: Impulse Response

To validate the model for temporal response (as opposed to frequency response) the flow field solution for impulse forcing in the  $y$  direction (Eq. (28)). the results are compared to the similar work done in M. R. Jovanovic, 2004

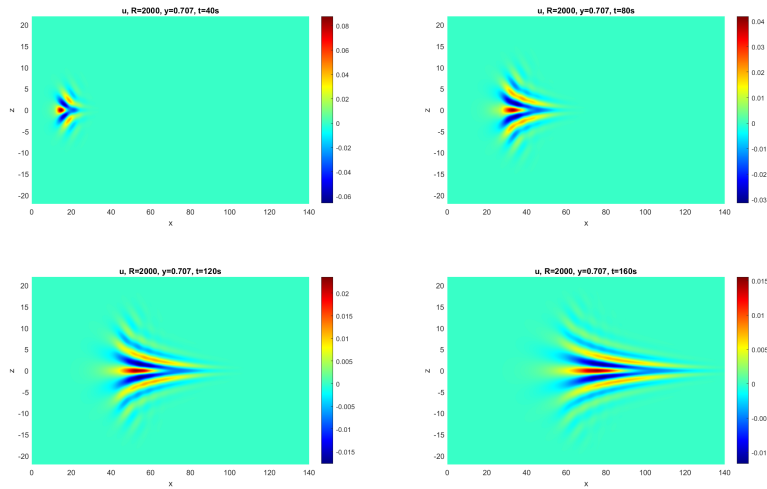


Figure 21: Streamwise velocity perturbation pseudo-color plots in the horizontal plane  $y \approx 0.71$  at:  $t = 40[s]$  (top left),  $t = 80[s]$  (top right),  $t = 120[s]$  (bottom left), and  $t = 160[s]$  (bottom right). Forcing in the  $y$  direction

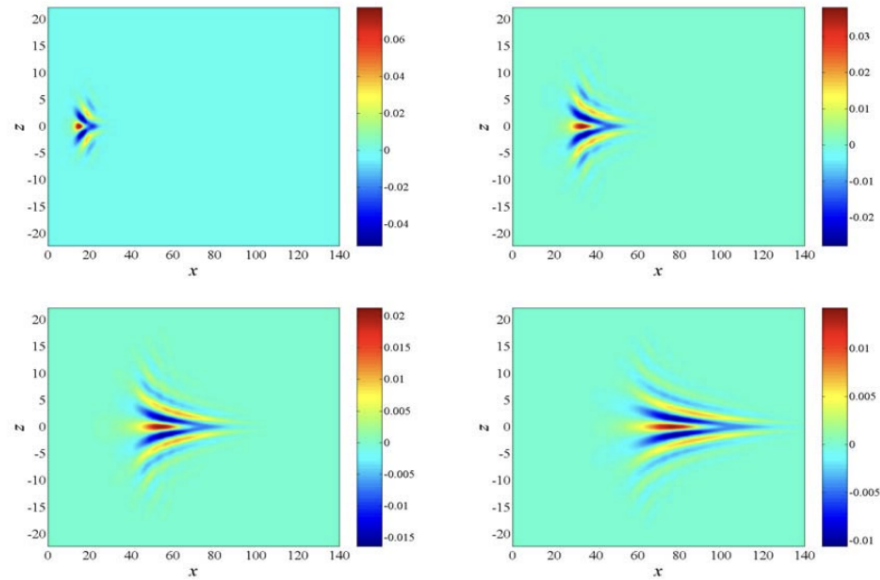


Figure 22: Streamwise velocity perturbation pseudo-color plots in the horizontal plane  $y \approx 0.68$  at:  $t = 40[s]$  (top left),  $t = 80[s]$  (top right),  $t = 120[s]$  (bottom left), and  $t = 160[s]$  (bottom right). Forcing in the  $y$  direction, Reprinted from Fig. 10.11 M. R. Jovanovic, 2004

## References

- Aghaee, P. K., Zilouchian, A., Nike-Ravesh, S., & Zadegan, A. H. (2003). Principle of frequency-domain balanced structure in linear systems and model reduction. *Computers & Electrical Engineering*, 29(3), 463–477.
- Belson, B., Meidell, K., Hanson, R., Palmeiro, D., Lavoie, P., & Rowley, C. (2012). Comparison of plasma actuators in simulations and experiments for control of bypass transition. *50th AIAA Aerospace Sciences Meeting including the New Horizons Forum and Aerospace Exposition*, 1141.
- Chavarin, A., & Luhar, M. (2019). Resolvent analysis for turbulent channel flow with riblets. *AIAA J.*, 1–11.
- Gluzman, I., & Gayme, D. F. (2021a). Input-output framework for actuated boundary layers. *Phys. Rev. Fluids*, 6, 053901.
- Gluzman, I., & Gayme, D. F. (2021b). Input-output framework for actuated boundary layers. *Physical Review Fluids*, 6(5), 053901.
- Hanson, R. E., Lavoie, P., Naguib, A. M., & Morrison, J. F. (2010). Transient growth instability cancelation by a plasma actuator array. *Experiments in fluids*, 49, 1339–1348.
- Hespanha, J. P. (2018). *Linear systems theory*. Princeton university press.
- Hwang, Y., & Cossu, C. (2010). Amplification of coherent streaks in the turbulent Couette flow: An input-output analysis at low Reynolds number. *J. Fluid Mech.*, 643, 333–348.
- Jordinson, R. (1970). The flat plate boundary layer. part 1. numerical integration of the orr–sommerfeld equation. *Journal of Fluid Mechanics*, 43(4), 801–811.
- Jovanovic, M., & Bamieh, B. (2001). The spatio-temporal impulse response of the linearized navier-stokes equations. *Proceedings of the 2001 American Control Conference.(Cat. No. 01CH37148)*, 3, 1948–1953.

- Jovanovic, M. R. (2004). *Modeling, analysis, and control of spatially distributed systems*. University of California, Santa Barbara.
- Jovanović, M. R., & Bamieh, B. (2005a). Componentwise energy amplification in channel flows. *J. Fluid Mech.*, 534, 145–183.
- Jovanović, M. R. (2021). From bypass transition to flow control and data-driven turbulence modeling: An input–output viewpoint. *Annual Review of Fluid Mechanics*, 53, 311–345.
- Jovanović, M. R., & Bamieh, B. (2005b). Componentwise energy amplification in channel flows. *Journal of Fluid Mechanics*, 534, 145–183.
- Kim, J., & Bewley, T. R. (2007). A linear systems approach to flow control. *Annu. Rev. Fluid Mech.*, 39, 383–417.
- Kim, J., Moin, P., & Moser, R. (1987). Turbulence statistics in fully developed channel flow at low reynolds number. *Journal of fluid mechanics*, 177, 133–166.
- Moarref, R., & Jovanović, M. R. (2010). Controlling the onset of turbulence by streamwise travelling waves. Part 1. Receptivity analysis. *J. Fluid Mech.*, 663, 70–99.
- Moarref, R., & Jovanović, M. R. (2012). Model-based design of transverse wall oscillations for turbulent drag reduction. *J. of Fluid Mech.*, 707, 205–240.
- Morra, P., Sasaki, K., Hanifi, A., Cavalieri, A., & Henningson, D. S. (2020). A realizable data-driven approach to delay bypass transition with control theory. *J. Fluid Mech.*, 883.
- Schmid, P. J., Henningson, D. S., & Jankowski, D. (2002). Stability and transition in shear flows. applied mathematical sciences, vol. 142. *Appl. Mech. Rev.*, 55(3), B57–B59.
- Semeraro, O., Bagheri, S., Brandt, L., & Henningson, D. S. (2013). Transition delay in a boundary layer flow using active control. *J. Fluid Mech.*, 731, 288–311.
- Smith, J. O. (2008). *Mathematics of the discrete fourier transform (dft): With audio applications*. Julius Smith.
- Taira, K., Brunton, S. L., Dawson, S. T., Rowley, C. W., Colonius, T., McKeon, B. J., Schmidt, O. T., Gordeyev, S., Theofilis, V., & Ukeiley, L. S. (2017). Modal analysis of fluid flows: An overview. *AIAA J.*, 55(12), 4013–4041.
- Thomas, F. O., Corke, T. C., Duong, A., Midya, S., & Yates, K. (2019). Turbulent drag reduction using pulsed-DC plasma actuation. *J. Phys. D: Appl. Phys.*, 52(43), 434001.
- Tol, H. J., de Visser, C. C., & Kotsonis, M. (2019). Experimental model-based estimation and control of natural Tollmien–Schlichting waves. *AIAA J.*, 57(6), 2344–2355.
- Weideman, J. A., & Reddy, S. C. (2000). A matlab differentiation matrix suite. *ACM transactions on mathematical software (TOMS)*, 26(4), 465–519.
- Zhou, K., Doyle, J. C., & Glover, K. (1995, August). *Robust and optimal control*. Pearson.